Charles University in Prague
Faculty of Mathematics and Physics

DOCTORAL THESIS

Andrii Lynnyk

Evolution of Interplanetary Coronal Mass Ejections

Department of Surface and Plasma Science

Thesis supervisor: RNDr. Marek Vandas, DrSc.

Doctoral thesis in branch F-2,
Physics of Plasma and Ionized Media

Prague 2011

Preface

This thesis has been accomplished at the Department of Surface and Plasma Science of the Faculty of Mathematics and Physics of Charles University in Prague.

First, I would like to thank my supervisors Dr. Marek Vandas and Prof. Zdeněk Němeček for their too much help with the research work that has become this thesis. Knowledge and skills wich I gained from them will be very helpful for my future work.

I wish to express my gratitude to Prof. Jana Šafránková who has been kind and generous to guide me through my PhD study. Her significant remarks greatly helped me to complete this thesis.

I want also to thank all professors of our Department and academic staff of Charles University who not only presents us with excellent theoretical knowlege, but also helped to solve practical questions during education process. I wish to especially thank to Dr. Lubomír Přech for his valuable advises in programming and great help with data accessing.

I would like to express my gratitude to my wife, Olya for her love, patience and understanding. Thanks to her I started and finished my PhD study in Charles University. She has always been a great support to me and motivation to move on.

I'm grateful to my parents for their love and support. And, of course, I would like to thank all my friends for splendid communication, understanding and support in hard times.

This thesis combines the results from several closely related studies of the evolution of interplanetary coronal mass ejections. In Chapter 1, we define present knowledge about ICMEs and MCs and discuss processes that may affect their shape. The aims of the thesis are presented in Chapter 2. In Chapter 3, we describe spacecraft measurements of the ICMEs and MCs. Since the coupling between the solar wind and the magnetosphere is controlled by the IMF orientation, Chapter 4 contains a study of different aspects of the ICME deformation.

This thesis was prepared under a support of the Research Plan MSM 0021620860 that is financed by the Ministry of the Education of the Czech Republic.

I declare that I carried out this doctoral thesis independently, and only with the cited sources, literature and other professional sources.

I understand that my work relates to the rights and obligations under the Act No. 121/2000 Coll., the Copyright Act, as amended, in particular the fact that the Charles University in Prague has the right to conclude a license agreement on the use of this work as a school work pursuant to Section 60 paragraph 1 of the Copyright Act.

In Prague, June 2011 Andrii Lynnyk

Abstract

Title: *Evolution of Interplanetary Coronal Mass Ejections*

Author: *Andrii Lynnyk*

Department: *Department of Surface and Plasma Science*

Supervisor: *RNDr. Marek Vandas, DrSc.*

e-mail address: *vandas@ig.cas.cz*

Abstract: *This thesis deals with deformation of the Interplanetary Coronal Mass Ejections (ICMEs) and their sub-class Magnetic Clouds (MCs) during their propagation in the Solar Wind (SW). The statistical study of the expanded MCs has shown that expansion greatly affects the MC internal magnetic field. We had shown that this influence is more clear for the MCs observed close to their axes. The study of the stand-off shock distance in front of the supersonic ICME confirms a smooth deformation of the ICMEs along their path from the Sun into interplanetary space. We observed that this deformation is increasing with the velocity of the ICME. This study also confirmed the difference in sheaths that are created in front of expanding and non-expanding ICMEs. We found that velocity distribution inside the MC is not uniform and it has large fluctuations. We found that the MC cross-section is usually strongly deformed.*

Keywords: *interplanetary coronal mass ejection, magnetic cloud, magnetosheath, flux rope, magnetic field, shock, fitting*

Abstract

Název práce: *Vývoj meziplanetárních koronálních výronů hmoty*

Autor: *Andrii Lynnyk*

Katedra: *Katedra fyziky povrchů a plazmatu*

Vedoucí disertační práce: *RNDr. Marek Vandas, DrSc.*

e-mail address: *vandas@ig.cas.cz*

Abstract: *Práce se zabývá deformací meziplanetárních výronů koronální hmoty (ICMEs) a jejich podskupiny, magnetických oblaků (MCs), během šíření slunečním větrem (SW). Statistické studium expandujících MCs ukázalo, že expanze velmi ovlivňuje jejich vnitřní magnetické pole. Ukázali jsme, že tento vliv je mnohem zřetelnější pro MC pozorované v blízkosti jejich os. Studium vzdálenosti rázove vlny před nadzvukovými ICMEs potvrzuje jejich postupnou deformaci během šíření od Slunce meziplanetárním prostorem. Dokázali jsme, že tato deformace se zvětšuje s roztoucí rychlostí ICME. Práce také potvrdila rozdíl v přechodove oblasti, která se vytváří před expandujícími ICMEs. Zjistili jsme, že rozdělení rychlostí uvnitř MC není rovnoměrné, ale má velké fluktuace. Dale jsme zjistili, že průřezy MCs jsou obvykle podstatně deformované.*

Klíčová slova: *Meziplanetární koronální výron hmoty, magnetický oblak, přechodová oblast, magnetický provazec, magnetické pole, rázova vlna, fitování*

Contents

Chapter 1

Introduction

1.1 Solar Wind

The Solar Wind (SW) is the solar atmosphere constantly expanding into the interplanetary space. It flows with a speed of about 400 km/s and a density of 5 1/cc at the Earth's orbit. The analytical solution for the expanded solar wind was performed by *Parker* (1958). The previous works based on the model of static isotermic solar atmosphere could not represent an equilibrium state between solar corona (outer region of the solar atmosphere) and the interstellar medium. *Parker* (1958) proposed the model of non-static isotermic solar atmosphere and obtained that the solar atmosphere slowly expands close to the Sun and constantly accelerates reaching the supersonic velocities on a height about 1.7 R_S. Unlike the surface of the Sun that has temperature about 6000 K, the solar corona has the average temperature about 10^6 K that gives the SW energy to escape the Sun's gravity. Figure 1.1 shows different profiles of the calculated SW velocity in dependence on the plasma temperature.

The SW consists of charged particles, mostly electrons and protons with a small amount of He^{++} (about 4-5%) and heavier ions (less than 0.1%). The density of the SW as well as ratio of its components may change as a result of different manifestation of local instabilities in the Sun, such as flares, coronal mass ejections etc, and may be the indication of theese processes.

The inhomogeneous rotation of the Sun and the convectional processes inside create the solar Magnetic Field (MF). The main component of the solar MF is dipole but during periods of the maximal solar activity, the higher components are prevailed. The average magnitude of the MF is 5 nT on the Earth orbit and it is decreasing with heliocentric distance as $1/R$ (because the magnetic energy proportional B^2 decreases as $1/R^2$). Due to a high temperature (up to $2{\cdot}10^6$ K), the SW plasma has very high conductivity and the coronal MF is "frozen in" and moving with the SW. The illustration of the MF configuration affected by the SW is shown in Figure 1.2a. There is a current sheet separating regions of an opposite magnetic polarity and extending outward into the interplanetary space.

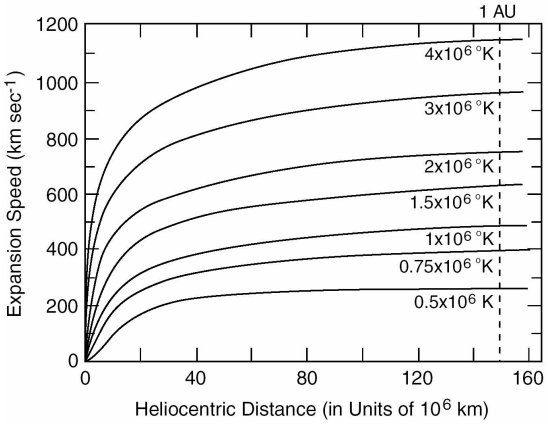

Figure 1.1: Profiles of the SW velocity for different values of the coronal temperature. Adapted from *Parker* (1958).

These features are the cause that the SW has lower values of the velocity near to the ecliptic plane (the so-called "slow" solar wind with the velocity of 300-500 km/s) where the plasma flows perpendicularly the MF than in higher heliospheric latitudes ("fast" solar wind with the velocity of 600-800 km/s) where the plasma propagates along open radial MF lines. The flow of the plasma at the ecliptic plane drags the magnetic field lines, bending them into so called streamer belt (in Figure 1.2, the idealized streamer belt is shown). In Figure 1.3, the distributions of the SW velocity and density on heliolatitude are shown. One can see that the SW at the low heliolatitude (less that 20°) has 2 times lower velocity and 3 times larger density.

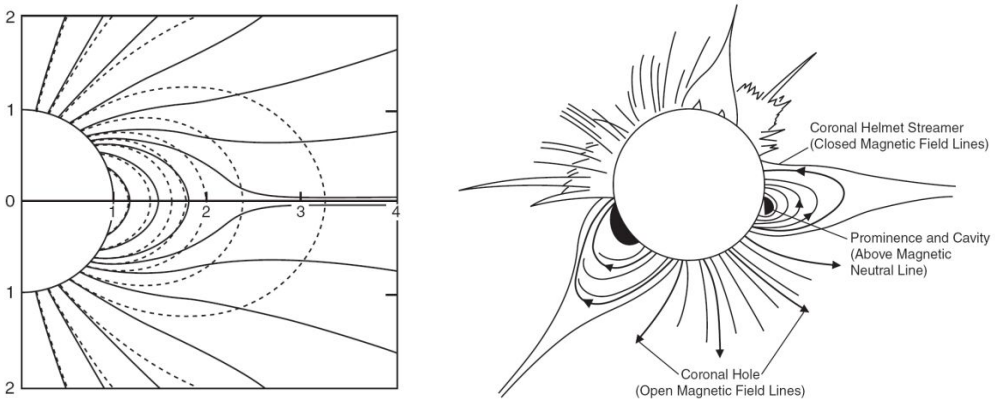

(a) (b)

Figure 1.2: (a) - Idealized three-dimensional view of the streamer belt and the coronal magnetic field (*Hundhausen*, 1977), and (b) - a more realistic sketch of the structure of the corona and its presumed magnetic field (*Kivelson and Russell*, 1995).

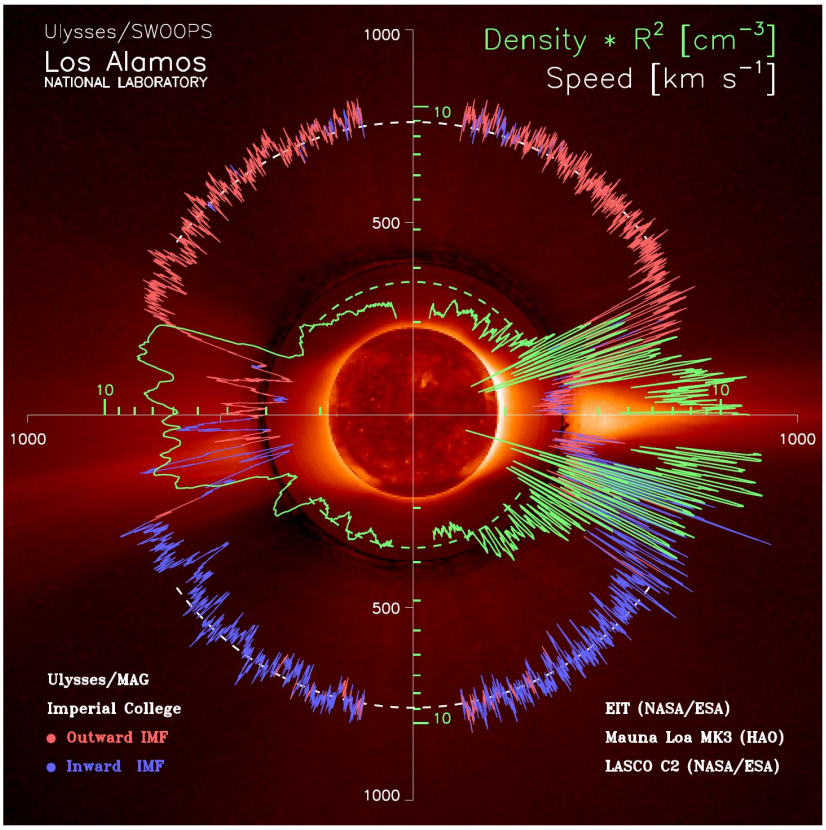

Figure 1.3: Distributions of the SW velocity and density on the heliolatitude. Adapted from *McComas et al.* (2000).

The real configuration is more complicated due to higher components in the solar MF and varies with the solar cycle. In Figure 1.2b, one of the possible magnetic configuration is shown. The coronal holes are the sources of the fast SW, while coronal streamers are the souces of the slow SW, probably with a higher density and a stronger magnetic field.

The fact that the streamer belt does not always lie in the ecliptic plane leads to the phenomenon of Corotating Interaction Regions (CIRs). The CIR is the region of the heliosphere where the faster SW propagates behind the slow SW, accelerating it and decelerating itself. There is often a CIR-induced shock on the boundary between the slow and fast region of the SW. One of the common features of the CIR-shock is the normal inclined about 45° to the X_{GSE} axis (the Sun-Earth line).

The other significant source of the global SW disturbance in the interplanetary space is represented by the Interplanetary Coronal Mass Ejections. They are large plasma structures (on order of $\sim$ 0.1-1 AU at the Earth orbit in different dimensions) that usually carry strong magnetic field and may create a shock in front of themselves. Their properties will be discussed through this section. In Table 1.1, the typical parameters of the SW at the Earth's orbit are shown.

Parameter	Minimum	Average	Maximum
Density (cm^{-3})	0.4	6.5	100
Helium %	0	5	25
Flow speed (km/s)	200	400	900
Magnetic field (nT)	0.2	6	80
Temperature (K)		$1.5 \cdot 10^5$	

Table 1.1: Average values of the solar wind parameters observed near the orbit of the Earth. Adapted from *Kivelson and Russell* (1995).

The interaction of the supersonic SW with the Earth magnetic field creates the magnetosphere (MS) with the bow shock (BS). Different processes in the SW may affect the Earth MS. The changing of the velocity, density or the magnetic field in the SW may cause the geomagnetic storms. The magnetic clouds usually carry the strong magnetic field and may propagate faster than the SW, being the source of the most severe geomagnetic storms.

1.2 Coronal Mass Ejections and Magnetic Clouds

The Coronal Mass Ejections (CMEs) are large plasma structures erupted from the Sun. They can be clearly seen by coronagraphs close to the Sun as they have larger density than the ambient corona with frozen-in magnetic field maintaining the form of CMEs. In Figure 1.4, the example of the observation of the CME taken with the LASCO (Large Angle and Spectrometric Coronagraph (*Brueckner et al.*, 1995)) on the SOHO spacecraft. CMEs are usually detected using coronagraphs on platforms either in the Earth orbit or near to the Earth (e.g., the L1 orbit). Such instruments being best suited to the detection of ejecta in the plane of the sky are capable to detect halo CMEs (the Earth-directed CMEs; they are usually covered by the coronagraph and do not exhibit recognizable structure), but these halo events are often rather weak in intensity. The better way of detecting the Earth-directed CMEs is provided by the STEREO mission (*Harrison et al.*, 2008) at present time. The STEREO spacecraft are travelling in the different direction along the Earth orbit and their spatial distributions allow them to observe Earth-directed CMEs on the limb.

It is well known that CMEs are associated with filament eruptions and solar flares (*Gosling*, 1990) and are supposed to have the form of the flux-ropes but the driver mechanism remains elusive. The scheme of mechanism for creating interplanetary magnetic ropes from arcades in the lower corona proposed by *Gosling* (1990) is shown in Figure 1.5. The initial arcade (top left scheme in the figure) after reconnection events transforms into the flux rope. The plasma slowly transfers to the flux rope along field lines. The instabilities that develop in the flux rope region lead to the eruption of the flux rope from the Sun.

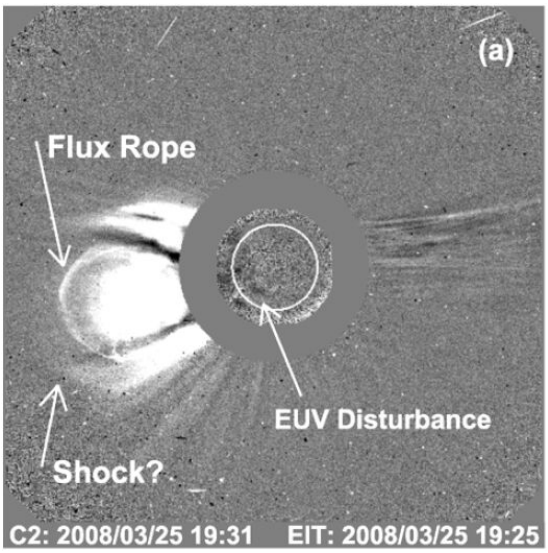

Figure 1.4: The 25 March 2008 CME when it first appeared in the LASCO/C2 field of view. The CME had a flux rope structure (marked) and a leading diffuse feature, whose outermost edge was interpreted as the shock. The EUV disturbance seen above the limb and on the disk coincides with the outermost part of the white-light disturbance that surrounds the flux rope. The velocity of the CME reached 1000 km/s in 1 hour after initiation (at a height of 10 R_S). Adapted from *Gopalswamy et al.* (2009).

Several theoretical models are described by *Krall et al.* (2001) within the context of the magnetic flux rope model of *Chen* (1996). These models include the flux injection, magnetic twisting, magnetic energy release and hot plasma injection (see Figure 1.6). The three-dimensional magnetic flux-rope model, in which a converging flow toward the neutral line results in reconnection beneath the flux-rope (*Forbes and Priest*, 1995) assumes that the kinematics of an erupting flux-rope can be described using a force-balance equation, which includes the gas pressure, gravity and Lorentz force. An alternative to this it is the magnetic break-out model in which the CME eruption is triggered by reconnection between the overlying field and a neighboring flux system (*Antiochos et al.*, 1999). The increased rate of outward expansion drives a faster rate of breakout reconnection yielding the positive feedback required for an explosive eruption. The models are dependent on geometrical properties of the CME, such as its width and radius, and they are designed to give an indication of the processes that drive the CME kinematics.

Byrne et al. (2009); *Wood and Howard* (2009); *Xie et al.* (2009) studied the CMEs close to the Sun using the STEREO mission, modeled and reconstruct them in a form of the flux rope or arc with the twisted MF inside.

At present, the most CME kinematics are derived from running difference images where each image is subtracted from the next one in order to highlight

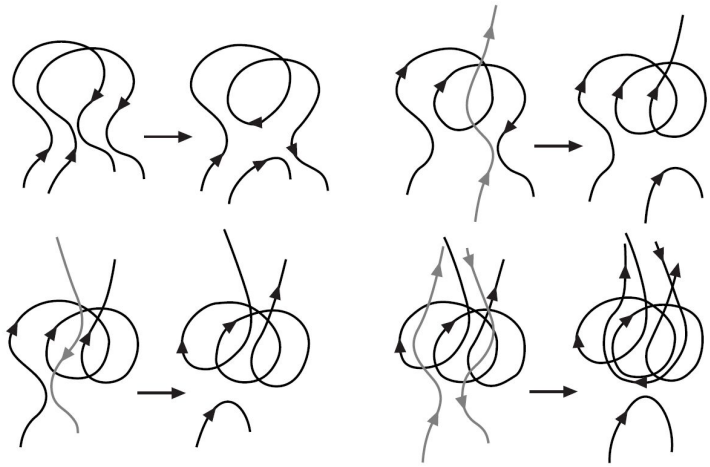

Figure 1.5: Proposed mechanism for creating interplanetary magnetic ropes from arcades in the lower corona. Adapted from *Gosling* (1990).

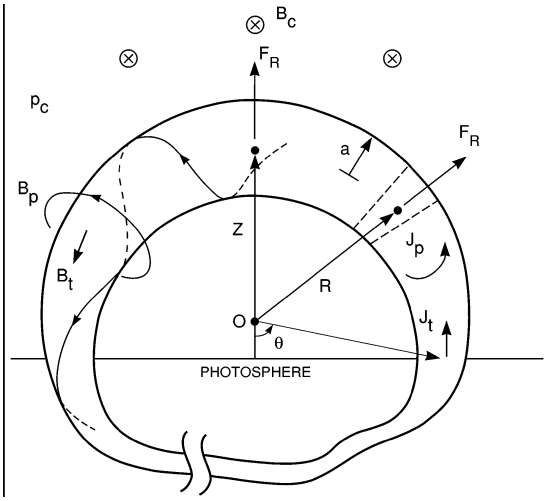

Figure 1.6: Model flux rope schematics. Subscripts p and t refer to the poloidal and toroidal directions, respectively. The ambient coronal field B_C is also indicated. Adapted from *Chen* (1989).

regions of changing intensity (*Byrne et al.*, 2009). Once the CME is identified, either manually through point-and-click estimates, or by a form of image thresholding and segmentation, height-time plots are produced and the velocity and acceleration of each event determined. CMEs are often thought of as being either gradual or impulsive depending on both their eruption mechanism (e.g., prominence lift off or flare driven) and their speed. The faster events tend to have an average negative acceleration attributed to aerodynamic drag of the SW (*Cargill*, 2004). It was also shown by *Gallagher et al.* (2003) that CMEs may undergo an early impulsive acceleration phase below $\sim 2R_{Sun}$.

Byrne et al. (2009) argued that the results of previous methods of the determination of the CME velocity and acceleration are limited mainly due to large kinematic errors which fail to constrain a model. Current methods fit either a linear model to the height-time curve implying constant velocity and zero acceleration or a second order polynomial producing a linear velocity and constant acceleration. *Byrne et al.* (2009) implemented a multiscale decomposition that provides a time error on the scale of seconds (the exposure time of the instrument) and a resulting height error on the order of a few pixels. The height-time error is used to determine the errors of the velocity and acceleration profiles of the CMEs. They confirmed that the previous constant acceleration model may not always be appropriate. Those CMEs that expand from the Sun with supersonic velocities comparable with the ambient SW produce the shock wave that is propagating prior to their edge. In Figure 1.4, an example of the CME with an induced shock is shown.

Those CMEs that are observed in the SW are now reffered as Interplanetary Coronal Mass Ejections (ICMEs). ICMEs in the SW can be determined by the one or several of following criteria (*Ebert et al.*, 2009; *Liu et al.*, 2005; *Neugebauer and Goldstein*, 1997; *Wimmer-Schweingruber et al.*, 2006; *Zurbuchen and Richardson*, 2006): at least twice colder protons compared to the ambient SW with the same velocity; higher helium concentration; the presence of suprathermal (<80 eV) counterstreaming electron beams; enhanced ion charge states; the stronger magnetic field with a smaller variance than in the ambient SW; low proton plasma β (<0.1); smooth and large rotation of the MF, cosmic ray decreases due to exclusion by the magnetic field.

The features that ICMEs exbitit lead to the assumption that ICMEs are large plasma structures with "frozen-in" helical magnetic field. The current paradigm of the ICME is shown in Figure 1.7, where the ICME in a form of a twisted flux rope connects to the Sun. However, at large distances, a connection of the ICME to the Sun is not verified.

A typical size of the ICME is about 0.07-0.6 AU along the X_{GSE} line at the Earth's orbit (*Lepping et al.*, 2006) and up to 6 AU at a heliocentric distance more than 10 AU (*Wang and Richardson*, 2004).

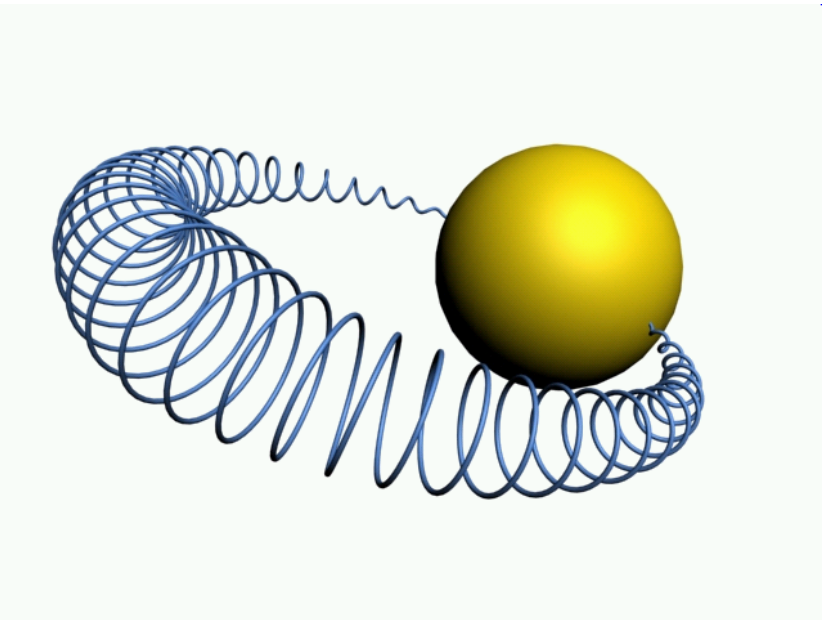

Figure 1.7: The current paradigm of a simple ICME or magnetic cloud in which a twisted flux rope connects back to the solar corona.

1.3 Models of Magnetic clouds

Magnetic clouds (MCs) are a sub-class of Interplanetary Coronal Mass Ejections (ICMEs) (the short review is made by *Démoulin* (2010)) with such satisfied features as the low proton temperature, low proton plasma β, and the strong magnetic field with a rotation up to about 180 degrees (*Burlaga et al.*, 1981).

In the magnetohydrodynamic (MHD) framework, the magnetic configuration of an MC can be obtained from the balance between the magnetic Lorentz force and the plasma pressure. Several magneto-static models have been used to describe the magnetic configuration of MCs.

When the plasma pressure is negligible compared to the magnetic pressure, the configuration is called "force-free" because the magnetic self-force is null (and so, magnetic field B is parallel to the electric current density, j), and the magnetic pressure is balanced by the tension of the curved magnetic field lines. The "linear force-free" field is a sub-set of solutions from the previous set, which satisfies $\nabla \times B = \alpha B$, with α constant in space. Here, we present four different cylindrical models, two force-free (one linear and one non-linear) and two non force-free.

The axially symmetric magnetic field corresponding to a linear force-free configuration was obtained by *Lundquist* (1950). It has been shown that this solution is consistent with *in situ* measurements of interplanetary magnetic flux ropes at

1 AU. Thus, the field of MCs is often relatively well modeled by

$$\begin{aligned} B_r &= 0, \\ B_\varphi &= B_0 J_1(\alpha r), \\ B_Z &= B_0 J_0(\alpha r), \end{aligned} \tag{1.1}$$

where J_0 and J_1 are the Bessel functions; $\alpha = const$; B_0 is the magnetic field strenght; r, φ and Z are cylindrical coordinates. The example of the fit of the magnetic cloud by April 22, 2001 by this model is shown in Figure 1.8.

Farrugia et al. (1999) proposed a non-linear force-free field with a uniform twist to model interplanetary flux tubes. For this configuration, B is given by *Gold and Hoyle* (1960) solution:

$$\begin{aligned} B_r &= 0, \\ B_\varphi &= \frac{B_0 br}{1+b^2r^2}, \\ B_Z &= \frac{B_0}{1+b^2r^2}, \end{aligned} \tag{1.2}$$

where $b = const$.

Hidalgo et al. (2000) proposed a non force-free model with the constant current density such as $j = [0, j_\varphi, j_Z]$ (with the components along $[r, \varphi, Z]$ of the cylindrical coordinate system), where j_φ and j_Z are constants. The magnetic field is:

$$\begin{aligned} B_r &= 0, \\ B_\varphi &= \frac{B_0 \tau r}{1-r/R}, \\ B_Z &= B_0(1 - r/R), \end{aligned} \tag{1.3}$$

where $\tau = const$; R is the MC radius.

A cylindrically symmetrical magnetic configuration with a current density such as: $j = [0, \alpha r, j_Z]$, with a and j_Z constants has been proposed for MCs by *Cid et al.* (2002). This structure has a magnetic field distribution given by:

$$\begin{aligned} B_r &= 0, \\ B_\varphi &= B_0 \tau r, \\ B_Z &= B_0(1 - r^2/R^2). \end{aligned} \tag{1.4}$$

A schematic illustration of the MC as a flux rope with helically twisted magnetic field lines is shown in Figure 1.9. The thin line in the XY_{GSE} plane shows a spacecraft trajectory through the MC. The distance from the MC axis Z_{MC} to this trajectory is called the "impact parameter" (it is usually measured in fraction of the MC radius). The magnetic field strength is maximal at the MC axis and decreases to its boundaries. Models usually determine the axial component of the magnetic field at the boundary to be zero (except for the *Gold and Hoyle* (1960) solution).

Dasso et al. (2006) performed the analysis of these models on the data obtained during observations of the MC registered on 18-20 October, 1995. They

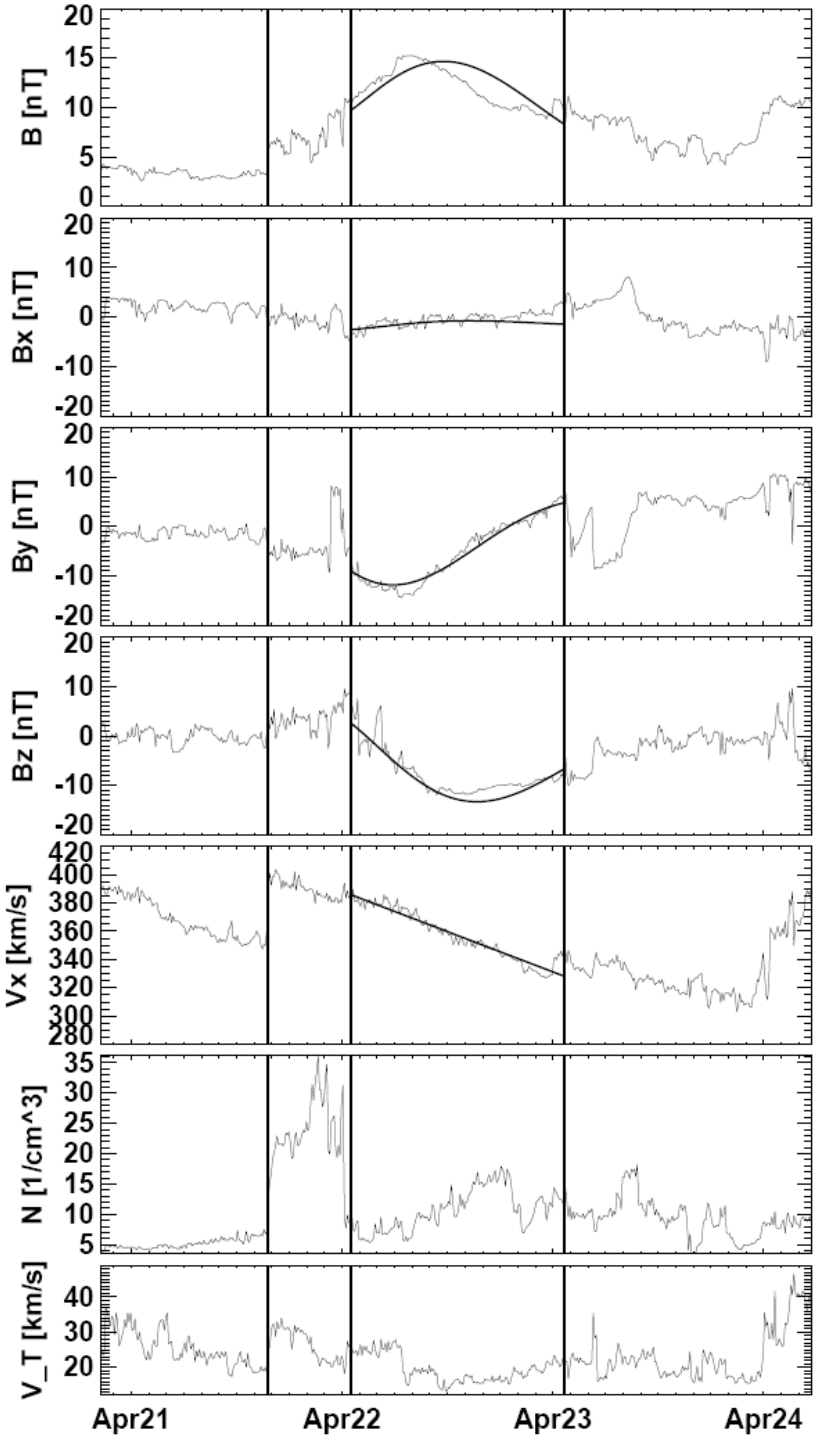

Figure 1.8: Example of the one MC seen by WIND on April 22, 2001. From top to bottom: strength and components of the magnetic field, $-Vx_{GSE}$ component of the velocity, proton number density, thermal velocity. The vertical lines represent the MC-driven shock and boundaries of the MC. The solid lines represent the magnetic field fit using the force-free model and a linear fit of the velocity. Adapted from *Lynnyk et al.* (2010).

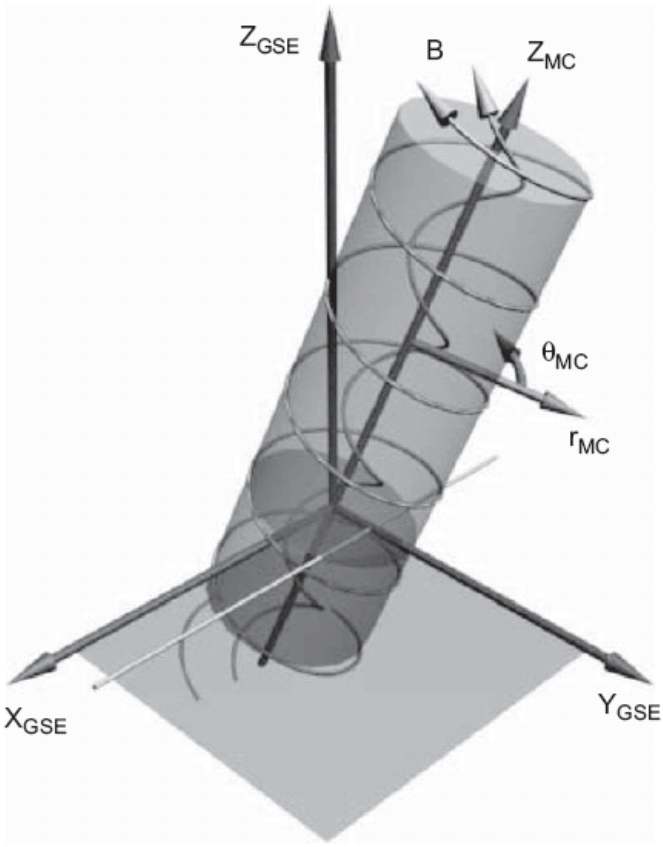

Figure 1.9: A schematic illustration of the MC model. The geocentric solar ecliptic (GSE) and MC coordinate systems are shown. The cylinder represents the MC body. The two coils represent magnetic field lines inside the cloud. The thin line in the XY_{GSE} plane shows a spacecraft trajectory during observations (*Lynnyk and Vandas*, 2009).

compare the residual functions $\chi^2 = \langle\left(\vec{B_{obs}} - \vec{B_{model}}\right)^2\rangle$ (where $\langle \ldots \rangle$ means averaging) for all four models and found the quality of their fits: models of *Cid et al.* (2002), *Hidalgo et al.* (2000), *Lundquist* (1950) and *Gold and Hoyle* (1960) are sorted in decreasing order. The magnetic fields of the MC obtained using their solutions are marked as "C", "H", "L" and "G", respectively, and are shown in Figure 1.10 as well as the observed magnetic field data. Despite of the arranging models by quality of the fits, one can see that the real data may have large fluctuations. For a more reliable conclusion, the statistical analysis with a large number of MCs is required. These models were used under consideration of MCs locally as steady-state cylinders.

There are several methods of the determination of the MC axis direction. Its orientation can be obtained by the minimization of the $\chi^2 = \langle\left(\vec{B_{obs}} - \vec{B_{model}}\right)^2\rangle$ function using of the models. It is possible to estimate the orientation of an

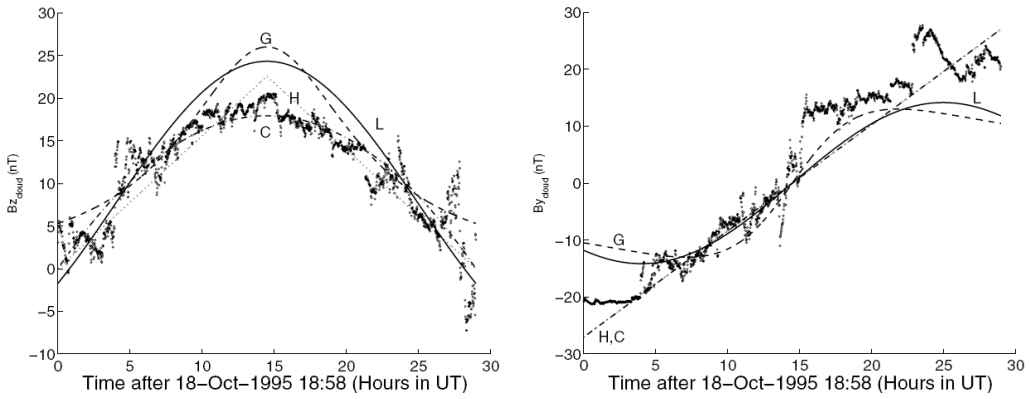

Figure 1.10: a) The axial component, $B_{z,cloud}$, of the MC magnetic field (local coordinate system obtained using mean variance analysis) as a function of time (in hours, after 18:58 UT, October 18, 1995); b) The field component in the direction orthogonal to both the spacecraft trajectory and MC axis. $B_{y,cloud}$ is the azimuthal component of the magnetic field with the hypothesis of negligible impact parameter. Dots correspond to the observed field (temporal cadence of one minute), solid line to the Lundquist model, dashed line to the Gold-Hoyle model, dotted line to the Hidalgo model and dash-dotted line to the Cid model. Adapted from *Dasso et al.* (2006).

MC applying the minimum variance (MV) method to the magnetic observations when the impact parameter is small compared to the MC radius. This method finds the directions ($\vec{n}$) in which the mean quadratic deviation of the field, $\langle(\vec{B}\cdot\vec{n}-\langle\vec{B}\cdot\vec{n}\rangle)^2\rangle$, is minimum and maximum, as well as the orthogonal direction to both. It is possible to show that this is equivalent to finding the eigen-vectors of the covariance matrix $M_{i,j}=\langle B_iB_j\rangle-\langle B_i\rangle\langle B_j\rangle$ (*Sonnerup and Cahill*, 1967). This symmetric and real matrix has three real eigen-values with orthogonal eigen-vectors. The MV method determines the MC axis direction, $\vec{\hat{z}}_{\rm cloud}$, as the eigen-vector associated with the intermediate eigen-value. The eigen-vector associated with the lowest eigen-value is expected to be close to the direction that results from the projection of the spacecraft trajectory on the plane perpendicular to $\vec{\hat{z}}_{\rm cloud}$. The eigen-vector associated with the highest eigen-value closes the system such that it is right handed.

Liu et al. (2007) have presented a method how to determine the magnetic field orientation of MCs based on Faraday rotation (FR). Their FR calculations, either with a simple flux rope or global MHD modeling, demonstrate the exciting result that the CME field orientation can be obtained $2-3$ days before a CME arrival at the Earth, which is substantially longer than the warning time achieved by local spacecraft measurements at L1. We should note that an actual CME likely shows a turbulent behavior with multiple structures along the line of sight. The interpretation of the FR measurements will be more complex. Therefore, the

study of the CME accompanied structures and specification of the CME structure is important for prediction of the geoeffectiveness of CMEs.

Later in the work, we will use the MC for describing such structures that have a distinct magnetic configuration (in form of a twisted spiral). Nevertheless, there is a lot of features that are observed for those ICMEs that are not suggested to be the MC. Thus, we will discuss all ICMEs irrespective of their structure together with MCs. We suppose their behavior to be similar in the most of cases.

1.4 Magnetic Cloud Expansion

MCs usually exhibit a smooth decrease of the velocity within its boundaries (see Figure 1.8) and this feature may be explained by their radial expansion (*Burlaga et al.*, 1990; *Farrugia et al.*, 1993).

Bothmer and Schwenn (1998) found that a radial diameter of the expanding MCs increases between 0.3 and 4.2 AU proportional to $R^{0.8}$ (where R is the heliocentric distance). Consistently with this expansion, the plasma density inside MCs decreases, faster than in the normal SW, proportional to $R^{2.4}$ between 0.3 and 1 AU. Further, *Démoulin and Dasso* (2009) found that MCs expand nearly self-similarly during their propagation from the Sun. They referred that radius of MCs increases linearly with the heliocentric distance.

The models that take the expansion effect into account consider either only a radial expansion (*Farrugia et al.*, 1993) or the expansion in both radial and axial directions (*Shimazu and Vandas*, 2002). *Vandas et al.* (2006) presented the fits of MC profiles by a force-free solution inside a circular cylinder with a flux rope expansion. *Marubashi and Lepping* (2007) used the technique of the least-square fitting to force-free flux rope models and compared both cylinder and torus models using the *Romashets and Vandas* (2003) model with modification that includes the expansion effect. These works are based on the study of the particular MCs and show better agreement between modeled and observed magnetic field for the model that takes expansion effect into account.

The magnetic field profile is not only one feature that changes with the expansion. It is known that supersonic MCs create the shock in front of them. But the shock in front of the MC may be formed not only by the supersonical propagation of the MC but also by its expansion. If the resulting velocity of the MC boundary is larger than the magnetosonic velocity (it may be caused by propagation and expansion), then the shock will be formed. *Siscoe and Odstrcil* (2008) have simulated and compared MCs and other heliophysical sheaths and shown that the sheath of expanding MCs (the so called the "expansion sheath" that forms around an object that expands but does not propagate relative to the solar wind) differs from the sheath formed by the propagation of steady-state MCs (the "propagation sheath"). The authors found that for the obstacles with a similar geometry the MC that expands will have two times thinner sheath than

one that only propagates (meaning the same velocities of their boundary relative to the medium). This result may be used as an additional feature in the study of the MC expansion. However, in the section 1.5, it will be shown that the MC deformation also may affect the sheath thicknesses. Thus, the correct study of the MC expansion should be performed together with the investigation of the MC deformation.

1.5 Magnetic Cloud Shape

The bidirectional flows of supra-thermal electrons along magnetic field lines that were observed inside MCs, support the assumption of closed field lines in agreement with observations that these plasma and magnetic field come in the solar wind from regions in the solar atmosphere where the magnetic field lines form closed loops (*Gosling et al.*, 1973). It has been proposed that the ejecta from CMEs evolves into large-scale magnetic flux ropes that remain magnetically connected to the solar atmosphere (*Gosling*, 1990). Observations of solar energetic particles (SEPs) associated with MCs (*Bothmer et al.*, 1996; *Farrugia et al.*, 1993) are in favor of this picture.

Larson et al. (1997) perform the analysis of the five solar impulsive $\sim 1 - 10^2$ eV electron events that were detected while the WIND spacecraft was inside the MC that was observed upstream of the Earth on October 18-20, 1995. The solar type III radio bursts produced by these electrons were directly traced from ~ 1 AU back to X-ray flares in solar active region AR 7912 implying that at least one leg of the cloud was magnetically connected to that region. Analysis of the electron arrival times showed that the lengths of magnetic field lines in that leg vary from ~ 3 AU near the cloud exterior to ~ 1.2 AU near the cloud center, consistent with a model force-free helical flux rope.

However, *Larson et al.* (1997) studied the topology of this cloud and suggested disconnection of magnetic field lines at one or both ends of the MC at least for the short ($\sim 1 - 2$ hours) periods. They studied the bidirectional streaming of the electons in the cloud at different energy ranges and found that the fluxes were comparable below ~ 200 eV but not above, consistent with both ends of the cloud field line being connected back to the solar corona, but to the regions of different coronal temperature. After 12 hours of the MC observations, the electon flux became generally uni-directional, indicating magnetic connection to the corona along only one leg of the cloud. Shortly ($\sim$3 hours) after that, the abrupt drops in the electron flux were observed. *Larson et al.* (1997) suppose that these features are evidences of the truly disconnection of the MC from the Sun.

As ICMEs have their own magnetic field, non-related to the ambient solar wind, they preserve their structure during propagation. Nevertheless, the interaction with the SW may affect the ICME in different ways. As ICMEs have the

pressure balance with the solar wind on own boundary, the decreasing of the SW pressure leads to their expansion. On the other hand, there is a drag force from the SW that affects ICMEs because they often have larger velocities than the SW. Also, due to large sizes, the ICME may be affected by the non-uniform SW if it is comparable with the streamer belt thickness (see Section 1.1).

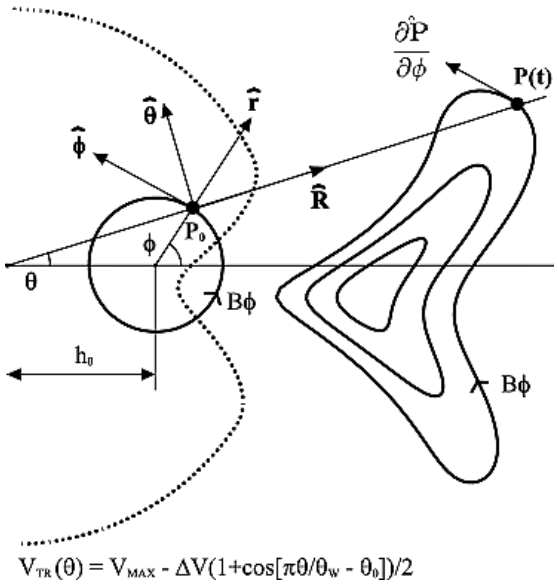

Figure 1.11: A schematic representation of the geometry used to generate the kinematically distorted flux rope model in a structured solar wind. A constant-α force-free flux rope is initially located at a heliocentric height h_0. Each point within the flux rope then moves subject to 2 velocities: antisunward (the $\hat{R}$ inline equation direction) at speed $V_{TR}(\theta)$ and antiaxially (the $\hat{r}$ direction) at speed V_{EX}. The dashed line shows the $V_{TR}(\theta)$ profile. Adapted from *Owens* (2006).

Owens (2006) modified an existing MC model based upon kinematically distorted flux ropes to include the effect of a structured solar wind, so as to give concave-outward structures thought to result from propagation into a solar minimum solar wind configuration. A robust signature of this concave-outward morphology was identified, and searched for in the spacecraft data. Three MCs were selected for their applicability to the analysis method and for their likelihood of forming concave-outward structures, due to both timing within the solar cycle and launch position. However, in all three cases, the convex-outward signatures (that correspond the simple uniform solar wind speed model) of the MC cross-section were fitted by the observation but not the expected concave-outward models. *Owens* (2006) supposed that the possible explanations of this unexpected result are: (1) the analysis methods used are not valid, and thus fail to detect the signatures of a concave-outward flux rope, and (2) the signatures of a concave-outward flux rope are not present in the *in situ* data (though the flux ropes may still be concave-outward on a global scale).

The analysis methods used in the study may be not valid to:

1. The flux rope axis is not correctly determined for the *in situ* observations. This seems unlikely as the field in the determined axial direction matches very well what was expected from the model (along with the good fit of the model in general). Furthermore, for two of the three events analyzed by *Owens* (2006), coronagraph and EIT observations suggest the magnetic clouds should be intercepted very close to the nose, and hence have axes perpendicular to the radial direction.

2. Effects of axial curvature are important and overwhelm the signatures of the MC distortion. For the apparent nose crossings selected by *Owens* (2006) for examination, the changes along the axial direction may be small compared to the changes perpendicular to the axis, and therefore the effect of curvature may be small.

3. Compression/rarefaction forces acting on the flux rope are not adequately taken into account beyond the added latitudinal dependence of the local transit speed.

There is also a possibility that signatures of a concave-outward flux rope exist but are not present in the data. The assumed explanation are:

1. Magnetic cloud distortion by a structured solar wind simply does not occur: magnetic clouds largely ignore the effect of a bimodal solar speed as the magnetic tension resists distortion. This strongly contradicts the results of multiple numerical simulations (*Owens*, 2006). It would suggest that magnetic tension forces are being severely underestimated. This effect would be more pronounced in MCs with very strong magnetic fields.

2. The speed variation at low latitudes required to provide the distortion is not present (i.e., the real solar wind speed is approximately uniform with latitude). Highly unlikely, as models of corona at this time suggest slow wind at low latitudes and fast wind from poles.

3. All three MC encounters were made at precisely the latitude of the solar wind speed minimum, and hence had no latitudinal speed gradient. This is statistically unlikely, and the fact that the observed radial fields are non-zero suggest this is not the case.

4. Distortion is not present in single spacecraft *in situ* data because the transition from fast to slow wind is sharp, allowing the parts of the flux rope in fast/slow wind to expand independently. The illustration of such structure is shown in Figure 1.12. The left (center) panel of Figure 1.12 shows the cross-sectional shape of a flux rope propagating through a uniform (structured) solar wind resulting in a convex- (concave-) outward flux rope. The

right panel shows a similar speed dip near the flux rope axis, but with a sharp latitudinal transition in speed. These results in the flux rope effectively breaking into separate latitudinal sections, which individually expand as per the uniform solar wind case. This would allow the flux rope structure to be concave-outward on a global scale, and thus drive shocks with a concave outward shape, but be convex-outward on a local scale, as measured by *in situ* observations.

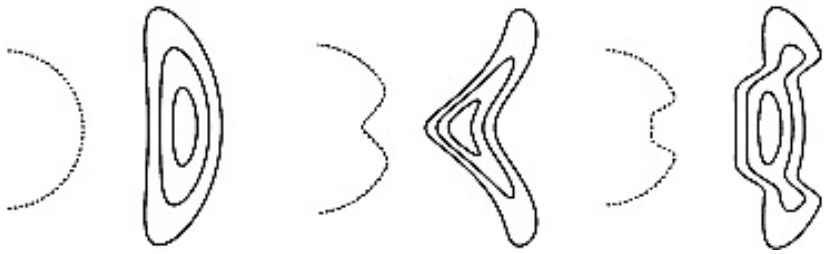

Figure 1.12: The flux rope cross-sections (solid lines) resulting from different speeds as functions of latitudes (dashed lines). The left panel shows the uniform solar wind case resulting in a convex-outward structure. The center panel shows a smooth dip in the speed near the axis of the flux rope, which leads to the concave-outward cross section. The right panel shows a similar dip in the speed close to the axis, but with a sharper transition from fast to slow wind. This results in a concave-outward structure on the global scale, but local *in situ* observations would reveal a convex-outward configuration of the flux rope field. Adapted from *Owens* (2006).

On the other hand, *Liu et al.* (2006) performed the study of the MC boundaries observed by ACE and Ulysses and have estimated a cross-section ratio to be larger than 6 : 1. They calculated the boundary normal of the MC and suggested that the MC cross-section is bended outward during the solar maximum and is bended inward during the solar minimum (Figure 1.13).

To obtain a measure of the transverse size, they used two spacecraft widely separated in the solar meridional plane. Launched in 1991, Ulysses explores the SW conditions at distances from 1 to 5.4 AU and up to 80° in latitude. Wind and ACE have provided near-Earth measurements (within 7° of the solar equatorial plane) since 1994 and 1998, respectively. *Liu et al.* (2006) looked for MCs in Ulysses data when it was more than 30° away from the solar equator. If the same MC was seen at the near-Earth spacecraft, then its transverse width is at least the spacecraft separation. To determine if the spacecraft observes the same MC, the timing and data similarities (similar transient signatures, the same chirality, etc.) were looked, and a one-dimensional (1-D) MHD model to do data alignment was used.

A direct consequence of the large transverse size is that MCs encounter different SW flows in the meridional plane. MCs can thus be highly distorted depending on the ambient solar wind conditions. The simplified scenario indicates

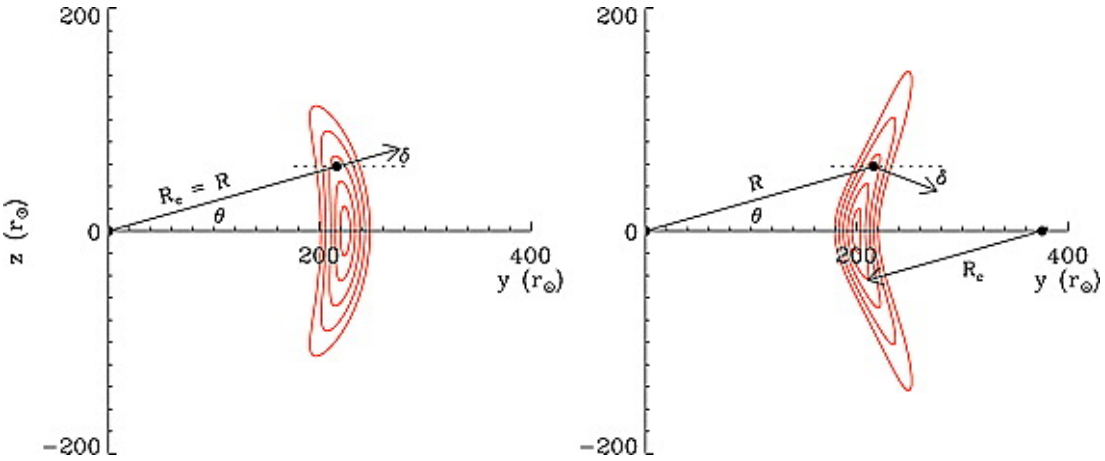

Figure 1.13: Schematic diagram of MCs at 1 AU in the solar meridional plane with an axis perpendicular to the radial and transverse directions, illustrating the large latitudinal extent and curvature in uniform (left, corresponding to solar maximum) and structured solar wind (right, corresponding to solar minimum). Contours denote levels of the initial flux-rope radius. The angles, labeled as θ and δ, represent the latitude of a virtual spacecraft and the elevation angle of the flux-rope normal. The distance of the spacecraft and radius of the flux-rope curvature are marked as R and R_c, respectively. Adapted from *Liu et al.* (2006).

that MCs should be ideally concave outward at the solar minimum and convex outward during the solar maximum. This curvature effect results in an inverse correlation between δ and θ at solar minimum and a positive correlation near solar maximum as shown in Figure 1.13. Note, however, that this is a greatly simplified picture. In reality, the shape of MCs will be determined by the speed at which they travel with respect to the background SW, ambient magnetic fields, the presence of other ICMEs or obstacles nearby.

We should note that the methods used by *Owens* (2006) and *Liu et al.* (2006) differ significantly and each of them has limitations that may corrupt the results. *Owens* (2006) fitted MCs using one spacecraft measurements and the limitation of this is discussed above. *Liu et al.* (2006) used the calculations of the MC boundary normals observed by two spatially and temporally separated spacecraft. As it will be discussed later, the MC boundary may be distorted and may not to be criterion for the determination of the MC orientation.

The other method of the study of the MC deformation is based on investigations of the properties of the shock that is created in front of the supersonical MCs. *Russell and Mulligan* (2002) performed the study of the ICME cross-section based on an estimation of the stand-off distance of the shock that is driven in front of the supersonical ICME. Such a supersonic ICME produces a standing shock wave in its frame. The plasma of the created magnetosheath flows around the ICME much as the plasma of the terrestrial magnetosheath flows around the Earths magnetosphere. The half-thickness of an ICME is typically 0.1 AU at 1

AU. As it is supposed, this dimension representing the characteristic scale size of the obstacle, leads to the thickness of the magnetosheath about 0.025 AU but, according to the observations, it is typically closer to 0.1 AU. *Russell and Mulligan* (2002) converted formula for the terrestrial magnetosheath thickness to one that is appropriate for the ICME sheath. They concluded that the characteristic radius of curvature of an ICME at 1 AU is about 0.4 AU. This radius of curvature is provided both by the bend of the rope axis and by an elongation of the ICME in the direction perpendicular to the rope axis and the SW flow. Thus, near 1 AU, ICMEs have a radial thickness that is smaller than their other two characteristic dimensions. This result is an additional confirmation of a deformation of the ICME from the circular shape.

Chapter 2

The aims of the thesis

As it follows from the previous chapter, ICMEs/MCs deform their shape on a path from the Sun mainly due to the expansion and to the drag force from the solar wind. The aim of this thesis is a study of the changes of ICME/MC cross-sections. We suppose following tasks:

1. A systematic study of the effectiveness of the MC expansion model. To fulfill it, we will compare the results of both the static and the expansion model (including a linear isotropic expansion) with observations of WIND MCs.

2. A study of the ICME/MC shape and its evolution along its path through the solar system. This study will be based on a detailed analysis of the thickness of sheaths in front of supersonic ICMEs;

3. An investigation of an anisotropic expantion of MCs leading to their elliptical cross-section. For this purpose, the model of expanding MCs will be modified and the results will be compared with experimental data.

In the thesis, the particular tasks are based on WIND and Voyager 2 observations of ICMEs/MCs during 1995-2011 and 1977-1989, respectively.

Chapter 3

Measurements of ICME/MC parameters

The analysis of MCs is based on the observations of the WIND spacecraft during 1995-2011. The analysis of such ICMEs that do not exhibit the MC structure is based on the observations of the Voyager 2 spacecraft during 1977-1989.

3.1 Wind spacecraft

Wind is a spin stabilized spacecraft launched in November 1, 1994 and placed in a halo orbit around the L1 Lagrange point more than 200 R_E upstream of the Earth to observe the unperturbed solar wind that impacts the Earth's magnetosphere.

The primary science objectives of the Wind mission were: (1) provide complete plasma, energetic particle and magnetic field for magnetospheric and ionospheric studies; (2) investigate basic plasma processes occurring in the near-Earth solar wind; (3) provide baseline, at 1 AU, ecliptic plane observations for inner and outer heliospheric missions.

The Wind Magnetic Field Investigation (MFI) is composed of two triaxial fluxgate magnetometers located at the mid point and end of a 12 m boom. The instrument provides (1) near real-time data at nominally one vector per 92 s as key parameter data for broad dispersion. (2) rapid data at 10.9 vectors s^{-1} for standard analysis, and (3) occasionally, snapshot memory data and Fast Fourier Transform data, both based on 44 vectors s^{-1}. The instrument features a very wide dynamic range of measurement capability, from ± 4 nT up to ± 65536 nT per axis in eight discrete ranges (*Lepping et al.*, 1995).

The Solar Wind Experiment (SWE) on the WIND spacecraft is a comprehensive, integrated set of sensors. It consists of two Faraday cup sensors; a vector electron and ion spectrometer (VEIS); a strahl sensor, and an on-board calibration system. The energy/charge range of the Faraday cups is 150 V to 8 kV, and that of the VEIS id 7 to 24.8 kV. The time resolution depends on the operation

mode used, but can be of the order of few seconds for 3D measurements (*Ogilvie et al.*, 1995).

3.2 Voyager Mission

The twin Voyager 1 and 2 spacecraft have been launched in August (Voyager 2) and September (Voyager 1), 1977 on a trajectory toward the upstream direction of the heliosphere, which was also toward the giant planets. After the successful planetary encounters, the Voyager Mission continued outward with the goal of making the first observations of the local interstellar medium (LISM). Both Voyagers have now crossed the termination shock, where the SW velocity changes from supersonic to subsonic. On August 2010, Voyager 1 was at a distance of 17.1 billion kilometers (114.3 AU) from the Sun and Voyager 2 at a distance of 13.9 billion kilometers (92.9 AU).

The identical Voyager spacecraft are three-axis stabilized systems that use celestial or gyro referenced attitude control to maintain pointing of the high-gain antennas toward Earth. The prime mission science payload consisted of 10 instruments (11 investigations including radio science). Only five investigator teams are still supported, though data are collected for two additional instruments.

The Voyager plasma experiment (PLS) registers solar wind protons simultaneously in three earthward-pointing Faraday cups over an energy range of 10–5950 eV with a time resolution of 192 s (*Bridge et al.*, 1977). When possible, the three spectra are fit with convected isotropic Maxwellian distributions to determine the proton velocity, density, and temperature. However, data quality often does not allow this fitting procedure.

The magnetic field (MAG) experiment carried on the Voyager 1 and 2 probes consists of dual low-field (LFM) and high-field magnetometer (HFM) systems (*Behannon et al.*, 1977). The dual systems provide greater reliability and, in the case of the LFM, permit the separation of spacecraft magnetic fields from the ambient fields. Additional reliability is achieved through electronic redundancy. The wide dynamic ranges of $\pm$ 5·10^4 nT for the LFM and $\pm$ 200·10^4 nT for the HFM, low quantization uncertainly of $\pm$ 0.002 nT in the most sensitive ($\pm$ 8 nT) LFM range, low sensor RMS noise level of 0.006 nT, and use of data compaction schemes to optimize the experiment information rate all combine to permit the study of a broad spectrum of phenomena during the mission.

3.3 Data selection

The MCs we used to our investigation were determined by *Lepping et al.* (2006). The authors identified the MCs from the meaturements of WIND and their analysis cover 1995-2003 years. Except for a few cases their MCs are revealed to be

generally large magnetic flux ropes in the SW, i.e., plasma embedded strong magnetic fields of approximally helical structure. The MCs were identified by visual inspectin of magnetic field and plasma data based on the *Burlaga* (1988) definition. *Lepping et al.* (2006) fitted the magnetic fields of selected MCs by a static force-free, cylindrically symmetric MC model (*Lepping et al.*, 1990) and provided seven relevant model fit-parameter values for each from 82 MCs. We checked these MCs and the MCs with data gaps were exluded from our further analysis. Furthemore, we enhanced this mentioned WIND database with MC observations registered during the 2007–2011 years for particular studies. These MCs and their boundaries were identified by their plasma β, magnetic field profile, plasma velocity and temperature.

The analysis of the ICMEs that do not exhibit the MC structure is based on the observations of the Voyager 2 spacecraft during 1977-1989. In 1977-1989, the Voyager 2 spacecraft flew from 1 to 30 AU. In this work, the 168 ICMEs determined by *Wang and Richardson* (2004) were analyzed and 26 ICMEs that met our requirements were selected for our processing.

Chapter 4

Evolution of ICMEs and MCs

4.1 Expansion of MCs

The velocity decrease that is often observed within MC boundaries led to presumption about expanding of the MCs (*Burlaga et al.*, 1990). We examined 82 MCs identified by *Lepping et al.* (2006) in order to select those that exhibit distinct monotonous decrease of the velocity during their observation, as it present in Figure 4.1.

To include the approximation of the self-consistent expansion to the MC model, we modified the force-free model (*Lundquist* (1950) solution) by a following way. The radial velocity of expansion, V^{exp} can be determined from the equation, $V^{exp} \cos\gamma \sin\phi = V^{border} - V^0$, where γ is the angle between the line from the observation point to the Sun and the line from the observation point to the MC axis; $\sin\gamma$ equals to the ratio of an impact parameter (distance from the MC axis to the spacecraft trajectory) over the MC radius, ϕ is an MC axis inclination angle, V^{border} is the velocity observed by the spacecraft at the leading edge of the MC, and V^0 is the velocity averaged through a whole time of the MC observation (*Osherovich et al.*, 1993); it is a close to the velocity of the MC center. We can describe the MC expansion using a new parameter, t_{exp} that characterizes the expansion rate and is defined according to *Lynnyk and Vandas* (2009) as:

$$t_{exp} = \frac{R_0}{V^{exp}}, \tag{4.1}$$

where R_0 is the MC radius at the time of the MC leading edge observation. We should note that we used only the X-component (in GSE) of the velocity for calculation of V^{exp} because fluctuations in the Y and Z components made the calculations more complicated.

The linear force-free solution given by Equation 1.1 may be modified by adding the time dependence of α and B_0 in a way (*Vandas et al.*, 2006)

$$\begin{aligned} \alpha &\rightarrow \frac{\alpha}{1+\frac{t}{t_{exp}}}, \\ B_0 &\rightarrow \frac{B_0}{1+\frac{t}{t_{exp}}}, \end{aligned} \tag{4.2}$$

We sorted 67 MCs from the *Lepping et al.* (2006) list and divided into two groups: non-expanding and expanding clouds. An example of both fitting procedures is shown in Figure 4.1 and one can see that the expanding model describes the observation much better than the static model.

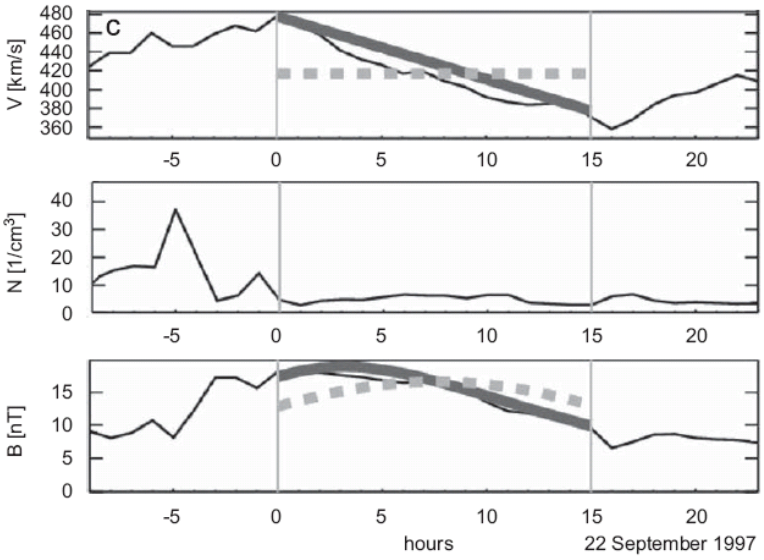

Figure 4.1: An example of fits of the velocity profile (top), solar wind density (middle) and magnetic field (bottom) within the MC boundaries. The magnetic cloud of 22 September 1997 exhibits the velocity decrease within its boundaries. The vertical lines show leading and trailing edges of MC and the time (in hours) on the horizontal axis is counted from the MC leading edge. In the top panel, the dotted line shows the average velocity; the solid line presents the linear fit of velocity. In the bottom panel, the dotted line shows the fit with the basic model (*Lundquist*, 1950), while the solid line shows the fit with the expansion model (*Shimazu and Vandas*, 2002).

To evaluate the effectiveness of the expansion model, we simulated magnetic fields of MCs observed by the spacecraft using both expansion and static models and compare the results with observed data. The deviations between observed and modeled magnetic fields were calculated as

$$\chi = \sqrt{\frac{\sum (B_X^O - B_X^M)^2 + (B_Y^O - B_Y^M)^2 + (B_Z^O - B_Z^M)^2}{N-1}}, \tag{4.3}$$

where B_X, B_Y, B_Z are GSE components of the magnetic field marked by O and M for observed and modeled fields, respectively, and N is a number of the data points

within the MC. The deviations calculated for fits of the expansion model (χ^{exp}) were compared with those calculated for the fits of the static model χ^{non_exp} using Equation 1.1. To estimate the applicability of the expansion model, we calculated improvement of χ (also mentioned as a reduction of χ) after an application of the new expansion model:

$$\chi \text{ improvement } = 100 \cdot (1 - \frac{\chi^{exp}}{\chi^{non\_exp}}), [\%]. \tag{4.4}$$

For the extended study, we calculated two χ values for the fitted magnetic field — one described of Equation 4.3 (later marked by χ_B) and the other one with the vectors of the magnetic field direction (with the unity length) used instead of the vectors of the magnetic field itself (later marked by χ_{dir}).

In Figure 4.2, the dependence of all χ improvements as a function of the expansion velocity is shown. The improvements were calculated for both the magnetic field, B (χ_B) and direction (χ_{dir}) deviations. One can see that both χ are generally improved for low values of the expansion velocity (up to $\sim$ 40 km/s) but for the larger expansion velocities the improvement of the χ values seems to be not dependent on the velocity. Moreover, the figure shows a large number of negative improvements. We can conclude that a linear dependence of the χ improvement on the expansion velocity for the lower values proves the correctness of the expansion hypothesis. We suppose that a large dispersion of the χ improvement at larger velocities is caused by the way of application of the expansion into the model.

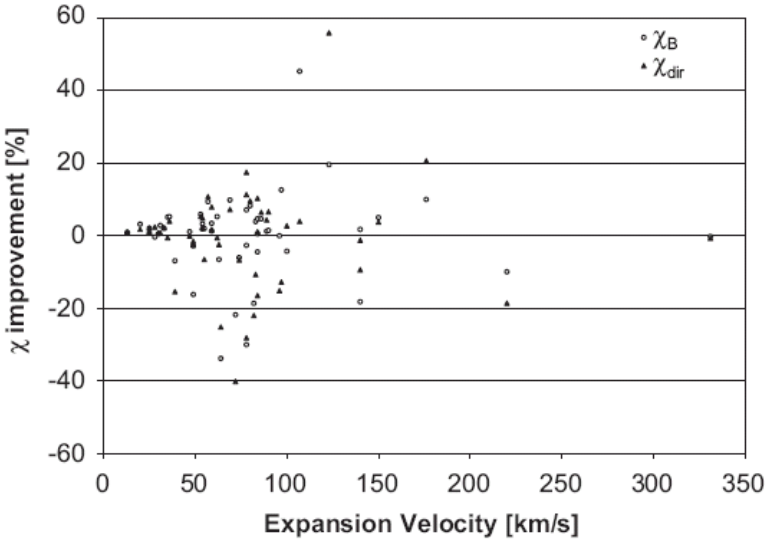

Figure 4.2: The distribution of χ improvements on the expansion velocity (V_{exp}). The improvements of both χ_{dir} (triangles) and χ_B (circles) are shown (*Lynnyk and Vandas*, 2009).

Thus, we perform a more accurate fitting of the MC magnetic field.

We involved an approximation of the self-consistent expansion into calculations of initial MC parameters. The fitting procedure is based on the minimization of $\chi^2 = \langle \Big(\vec{B_{obs}} - \vec{B_{model}})^2 \rangle$ (where $\langle \ldots \rangle$ means averaging). To minimize this function, we used the following set of the parameters that describe the MC: the axial magnetic field, axis direction, radius, and the impact parameter. In every iteration, we modified modified these parameters one by one with a small deviation and calculated the χ^2 value for every set. Obtained values were compared with those obtained for the original set of the MC parameters. For the next iteration, MC parameters were changed with fixed addendum. The sign of this addendum was selected to minimize the χ^2 value calculated for the set with modification of the corresponding parameter. We should note that these values were changed with fixed addendum in order to avoid the extension of the computation time.

There is a problem of local minima in the χ^2 function on the space of the MC parameters. This problem was avoided using several independent computations with different initial parameters. We have taken these initial parameters as points in the range of possible reasonable values of these parameters with the fixed length one from another. At the end of computations, the MC parameters corresponding to the minimum χ^2 value were selected.

Figure 4.3 shows an example of our new fit (solid line) and its comparison with the fit by the static model (dashed line). One can note that the expansion fit matches the experimental data better than the static model. The expansion leads to the non-symmetric profiles of magnetic field components with respect to the center of the observation interval and this feature is often recorded. In this case, the improvement is 32%, V^{exp} is 52 km/s, ϕ, θ angles of the MC axis inclination are 158° and 50° respectively, impact parameter, CA is 10%, MC radius is 0.084 AU and the axial magnetic field is 22.2 nT.

The statistics of new fit improvements brings Figure 4.4 that shows plots of the χ improvement as a function of the expansion velocity

We should note that the expansion velocity that we put into fitting procedure wasn't the additional free parameter. The expansion velocity was calculated from the fit of the velocity within MC boundaries.

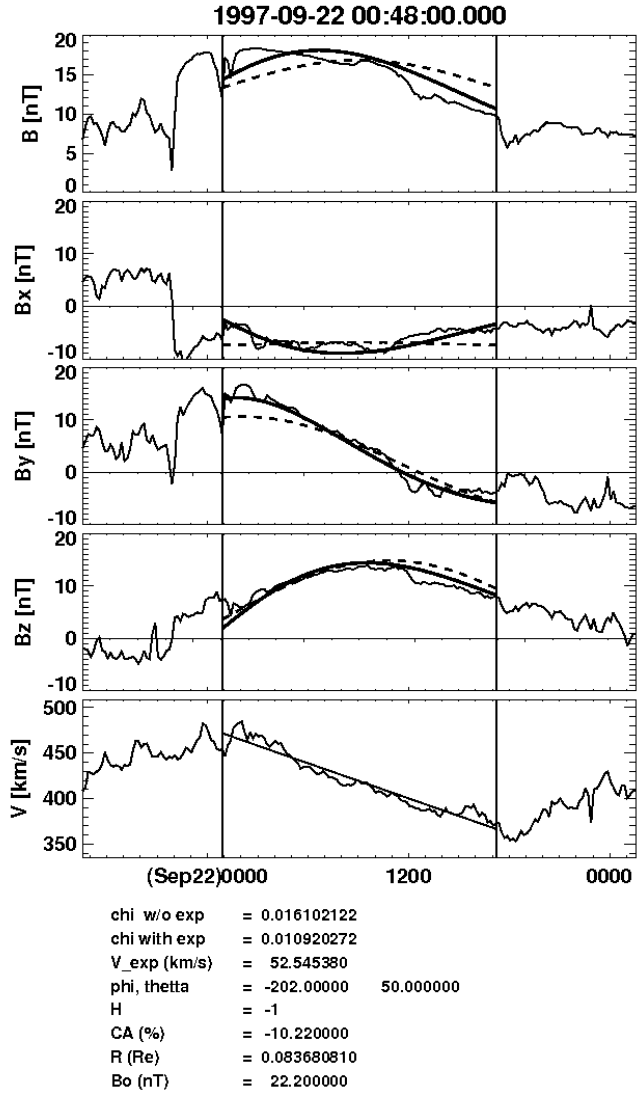

Figure 4.3: The MC on September 9, 1997. Magnitude and components (in GSE) of the magnetic field, and -X-component (in GSE) of the solar wind velocity are plotted. The vertical lines indicate an estimation of MC boundaries. The dashed lines show the fit by the classical Lundquist solution (Equation 1.1) and the solid lines stand for the fit including the MC expansion (Equation 4.2). The parameters of the MC yielded by the expansion model are given in the bottom part: the χ values (for the models without and with expansion), expansion velocity, ϕ and θ angles of the MC axis inclination, helicity, impact parameter, CA, the MC radius and the axial magnetic field (*Lynnyk and Vandas*, 2010).

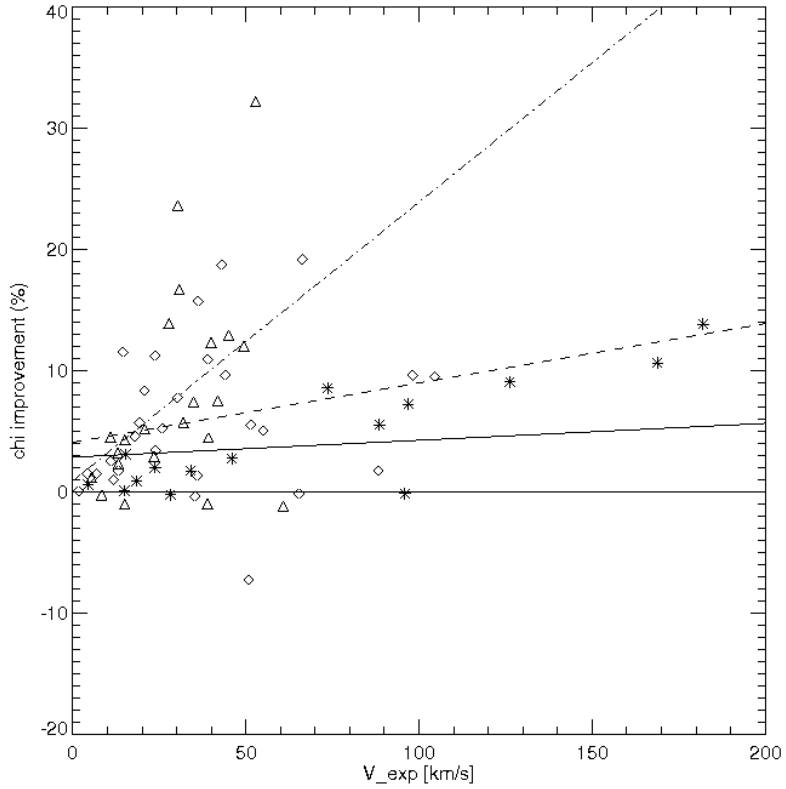

Figure 4.4: Improvements of fits of 68 MCs with the expansion model. All events were divided into 3 groups according to their CA: squares, approximated by solid line, with CA>85%; crosses (gray dashed line) with 50%<CA<85%; and stars (light gray dashed line) with CA<50% (*Lynnyk and Vandas*, 2010).

4.2 Study of elliptical MC cross-section

Despite of the fact that the magnetic field in flux ropes are often simulated by a force-free solution with constant alpha in a circular cylinder, MHD simulations and experimental investigations indicate that their cross-section is not circular but they are oblate due to interaction with the surrounding solar wind (e.g., *Lynnyk and Vandas*, 2010; *Vandas and Romashets*, 2003).

We use the solution of *Vandas and Romashets* (2003) of the force-free field with constant alpha in an elliptical MC. The basic force-free equation

$$\nabla \times B = \alpha B \tag{4.5}$$

is solved in the elliptic cylindrical coordinates u, v, and Z. These coordinates are defined by

$$\begin{aligned} x &= c\cosh(u)\cos(v), \\ y &= c\sinh(u)\sin(v), \\ z &= Z; \end{aligned} \tag{4.6}$$

where $c = \sqrt{a^2 - b^2}, u \in [0; +\infty)$, and $v \in [0; 2\pi]$. Contours with $u = const$ are ellipses. The generating ellipse ($u = u_0$) with the semimajor axis a and semiminor axis b has $\cosh(u_0) = a/c$ and its foci are at the points $(\pm c, 0)$ in the xy plane. The Lamé coefficients are $h_u = h_v = c\sqrt{\cosh^2(u) - cos^2(v)}$ and $h_Z = 1$.

Equation 4.5 in elliptic cylindrical coordinates has the components

$$\begin{aligned} \frac{1}{h_u}\frac{\partial B_Z}{\partial v} &= \alpha B_u, \\ -\frac{1}{h_u}\frac{\partial B_Z}{\partial u} &= \alpha B_v, \\ \frac{1}{h_u^2}\left(\frac{\partial}{\partial u}(h_u B_v) - \frac{\partial}{\partial v}(h_u B_u)\right) &= \alpha B_u, \end{aligned} \tag{4.7}$$

if we assume that the searched magnetic field does not depend on Z.

A substitution for B_u and B_v from Equation 4.7 into the equation for B_Z yields

$$\frac{\partial^2 B_Z}{\partial u^2} + \frac{\partial^2 B_Z}{\partial v^2} = -\alpha^2 c^2(\cosh^2(u) - \cos^2(v))B_Z. \tag{4.8}$$

From the expected behavior of the magnetic field inside a flux rope, we can assume that projections of magnetic field lines onto the xy plane coincide or is similar to ellipses and symmetrical in quadrants of the xy plane, and thus:

$$\begin{aligned} &B_x(x, 0, z) = 0, \quad B_y(-x, 0, z) = -B_y(x, 0, z), \\ &B_y(0, y, z) = 0, \quad B_x(0, -y, z) = -B_x(0, y, z). \end{aligned} \tag{4.9}$$

We assume that the flux rope has the shape of the generating ellipse, thus we solve (4.8) by a method of a separation of variables and denote

$$\varepsilon = (\alpha c)^2. \tag{4.10}$$

Let us assume that

$$B_Z = B_0 U_\varepsilon(u) V_\varepsilon(v), \tag{4.11}$$

where $U_\varepsilon(u)$ and $V_\varepsilon(v)$ are new functions (depending implicitly also on ε, which is stressed by the subscript), $V_\varepsilon(v)$ is periodic with the period π. We can put without loss of generality

$$U_\varepsilon(0) = 1; \quad V_\varepsilon(0) = 1 \tag{4.12}$$

The other components of Equation 4.7 are expressed

$$\begin{aligned} B_u = \frac{1}{\alpha h_u}\frac{\partial B_Z}{\partial v} &= \frac{B_0}{\alpha h_u} U_\varepsilon(u) V'_\varepsilon(v), \\ B_v = \frac{1}{\alpha h_u}\frac{\partial B_Z}{\partial u} &= \frac{B_0}{\alpha h_u} U'_\varepsilon(u) V_\varepsilon(v). \end{aligned} \tag{4.13}$$

At the boundary, $u = u_0$, it must hold for all v

$$B_u(u_0, v) = \frac{B_0}{\alpha h_u} U_\varepsilon(u_0) V'_\varepsilon(v) = 0, \tag{4.14}$$

therefore

$$U_\varepsilon(u_0) = 0. \tag{4.15}$$

This condition yields $B_Z = 0$ at the boundary (Equation 4.11).

With Equation 4.11, Equation 4.8 splits into two equations

$$\begin{aligned} U'' - (K_\varepsilon - \varepsilon \cosh^2 u) U'_\varepsilon &= 0, \\ V'' - (K_\varepsilon - \varepsilon \cos^2 v) V'_\varepsilon &= 0, \end{aligned} \tag{4.16}$$

where K_ε is a constant used in the separation of variables method. K_ε for a given ε is expressed by an infinite fraction

$$\begin{aligned} K_\varepsilon &= \frac{\varepsilon}{2} + \frac{\varepsilon^2}{8}\frac{\delta_2}{\delta_1}, \\ \frac{\delta_n}{\delta_{n+1}} &= K_\varepsilon - \frac{\varepsilon}{2} - 4n^2 - \frac{\varepsilon^2}{16}\frac{\delta_{n+2}}{\delta_{n+1}} \end{aligned} \tag{4.17}$$

For the calculation of K_ε the fraction is cut at some level and K_ε is found by a method of bisections.

For the computation purposes we present the solution of Equation 4.16 in the form of series. The substitutions $w = \sin^2 v$ and $s = \tanh^2 u$ changes 4.16 into

$$\begin{aligned} 4s(1-s)^3 U'' + 2(1-s^2)(1-3s)U' - (K_\varepsilon - \varepsilon - \varepsilon s)U &= 0, \\ 4w(1-w)V'' + 2(1-2w)V' + (K_\varepsilon - \varepsilon + \varepsilon w)V &= 0. \end{aligned} \tag{4.18}$$

The solution of Equation 4.18 is

$$\begin{aligned} U_\varepsilon(s) &= \sum_{n=0}^{\infty} b_n s^n, \\ V_\varepsilon(w) &= \sum_{n=0}^{\infty} a_n w^n. \end{aligned} \tag{4.19}$$

With equating coefficients at w^n in Equation 4.18, we get

$$\begin{aligned} b_1 &= \frac{(K_\varepsilon - \varepsilon)b_0}{2}, \\ b_2 &= \frac{(10 + K_\varepsilon - \varepsilon)b_1 - K_\varepsilon b_0}{12}, \\ b_n &= \frac{B_1 + B_2 + B_3}{2n(2n-1)}, \\ a_1 &= -\frac{(K_\varepsilon - \varepsilon)a_0}{2}, \\ a_n &= \frac{\mid 4(n-1)^2 - K_\varepsilon + \varepsilon \mid a_{n-1} - \varepsilon a_{n-2}}{2n(2n-1)}, \end{aligned} \tag{4.20}$$

where $B_1 = (2(n-1)(6n-7) + K_\varepsilon - \varepsilon)b_{n-1}$, $B_2 = K_\varepsilon)b_{n-2}$ and $B_3 = 2(n-3)(2n-5)b_{n-3}$.

According to Equation 4.12 $a_0 = 1$, $b_0 = 1$. An example of the magnetic field lines for the solution with $a/b = 3$ is shown in Figure 4.5.

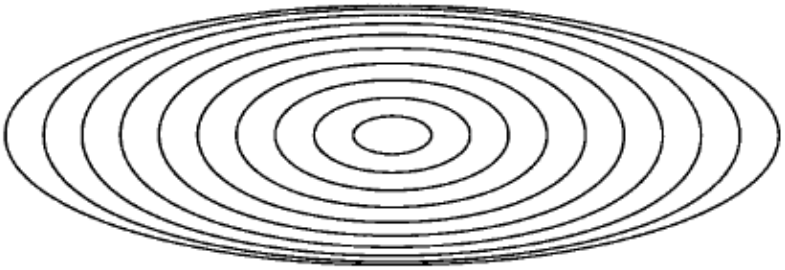

Figure 4.5: Magnetic field lines for the case of $a/b = 3$. The flux rope boundary is the generating ellipse. Adapted from *Vandas and Romashets* (2003).

We simulated MCs observed in 1995-2003 to evaluate the typical ratio of thir cross-sections. We used *Lepping et al.* (2006) timing of the MC observation and performed the fitting procedure on the whole set of MCs. For this study we used the model of the MC with elliptical cross-section described above. We perform the fitting procedure with minimization of the function $\chi^2 = \langle \left(\vec{B_{obs}} - \vec{B_{model}})^2 \right\rangle$ (where $\langle \ldots \rangle$ means averaging) with the following parameters: ratio of the semi-axes of the elliptical MC, axial magnetic field, "cone" and "clock" angles of the

MC axis, distance from the MC axis to the spacecraft. The spatial orientation of the MC cross-section was selected so that larger semi-axis, a was orientated orthogonal to X_{GSE}.

In order to avoid unnecessary computation, we divided the fitting procedure into two steps. During the first step, the set of the magnetic configurations corresponding to the different MC cross-sections were computed. These configurations were characterized by the a/b ratio (the ratio of the semi-axes of the elliptical MC cross-section). As the *Vandas and Romashets* (2003) model is multiplicative in the MC axes and the axial magnetic field, we set these values to unity. Equation 4.20 were solved using a bisection method. During the second step of the fitting, every magnetic configuration was translated into the coordinate system rotated in the GSE system with the fixed angles ("cone" and "clock" angles of the MC axis), that correspond to the MC axis inclination. The obtained magnetic configuration was scaled to the observed MC size. Then, the magnetic field was multiplied by a variable coefficient and points corresponding to the fixed spacecraft trajectory were taken. After this, the χ^2 function of the difference of this field from observed was calculated.

The results of the procedure are shown in Figure 4.6. One can see the majority of MCs exhibits the semi-axes ratio (a/b) in a range of $1 - 1.6$ and several cases with a/b about 2.5. From this follows that a study of the deformation of MCs using the elliptical model does not bring significant enhancement of the development of the MC models. We believe that, despite of the improvement of the fits of the particular MC, this fitting procedure should not be used without the consideration of an additional manifestation of the MC deformation, such as MC-sheath thickening or the boundary normal study. The reason is that adding two semi-axes instead of one radius increases the number of free parameters (those that we are selecting in order to minimize the deviation between observed and modeled magnetic fields). Thus, the fit of the elliptical MC cannot be worse than the fit of the cylindrical MC (it is the same in the case of the equal semi-axes).

For this reason, we performed the study of the shape of those MCs that exhibit the expansion. We expect the expansion velocity to be axially symmetric for the cylindrical MC and embody an increase of the velocity component directed along a larger semi-axis. We calculated the value of the expansion velocity along the line perpendicular to X_{GSE} and the MC axis. This velocity is marked as Vx_ort in Figure 4.7. In Figure 4.8, the dependence of the expansion velocity perpendicular to the X_{GSE} axis as a function of the expansion velocity along the X_{GSE} line is shown.

As it is seen from Figure 4.8, the velocities are proportional for these MCs that are less deformed (semi-axis ratio is less than 1.4) but there is no dependence for highly deformed MCs. One of the possible explanations is that such distortion of the flattened MCs affects their magnetic field and makes impossible to evaluate the impact parameter through a fitting procedure. The other possible reason is that the distortion of MCs affects the velocity profiles. This is partially

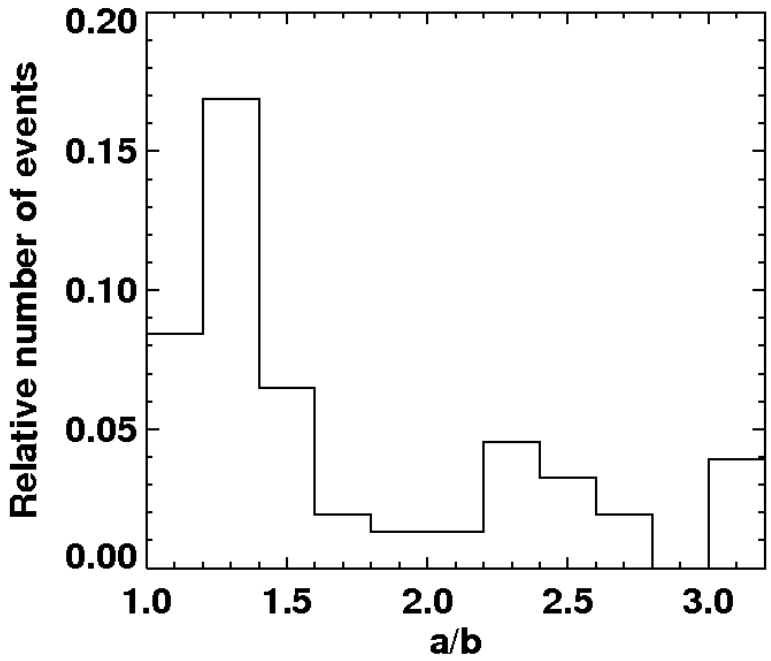

Figure 4.6: The distribution of the ratio of the semi-axes (a/b) of the MC cross-section.

shown in Figure 4.7 where Y_{GSE} and Z_{GSE} components of the velocity are highly fluctuating. Finally, the third possibility that would be investigated is a propagation of Alfvénic waves along the MC axis. Such waves would modulate the velocity component perpendicular the MC axis. We tried to take into account this last explanation. We modulated the X_{GSE} and Y_{GSE} components of the velocity according to fluctuations of corresponding magnetic field components (the red lines in Figure 4.8) but, unfortunately, the resulted velocity does not exhibit any reasonable dependence.

The study of the velocity profile within the MC reveals its large fluctuations. These fluctuations do not exhibit any reasonable dependence on the MC expansion or shape of its cross-section. The possible explanations are the non-uniform distortion of the MC that affects the velocity as well as the magnetic field profile or the waves that propagate along the MC axis. The study of distribution of the MC internal velocity may be used in global MHD MC models that take into account all these effects.

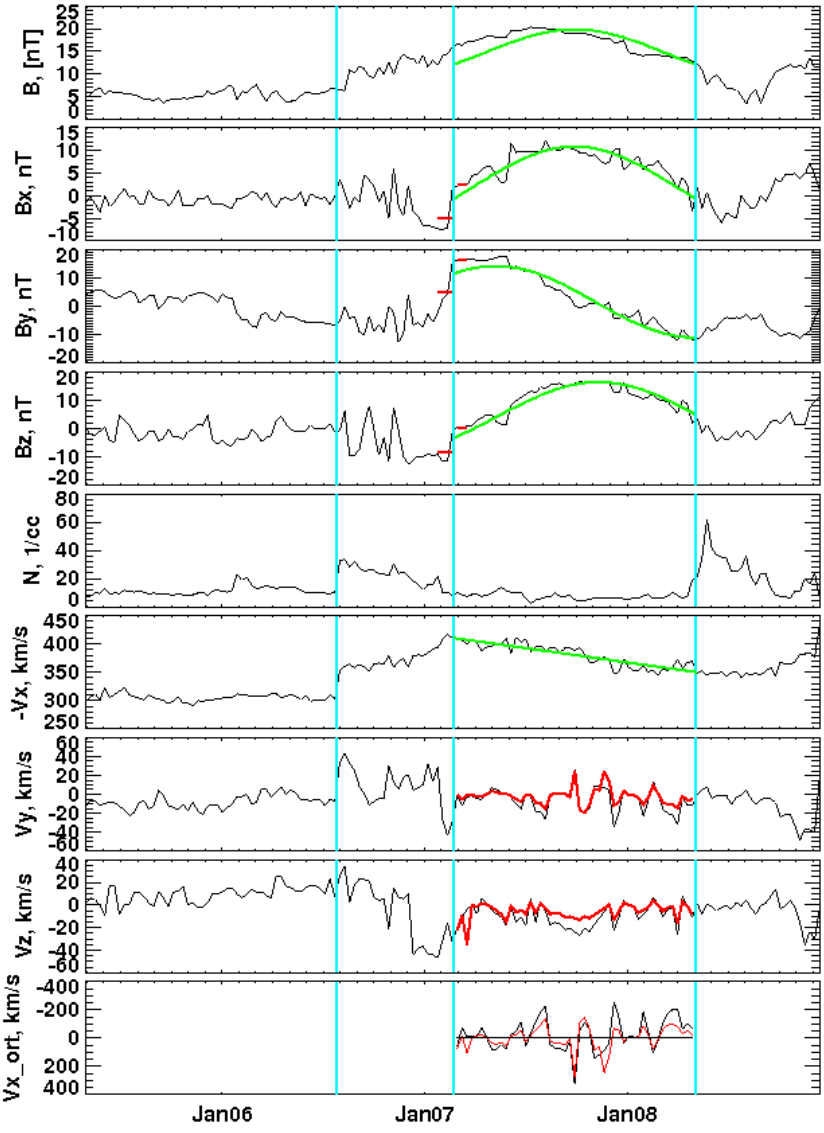

Figure 4.7: The example of the MC observed by the WIND spacecraft. From top to bottom: magnitude and components (in GSE) of the magnetic field, proton density, three components of the plasma velocity and the velocity in the orthogonal direction. The red velocity profiles indicate the velocity modulated by the MF relative deviations (between observed and modeled magnetic fields). The short red lines at the MC boundary indicate average magnetic field components used for determination of the MC boundary normal.

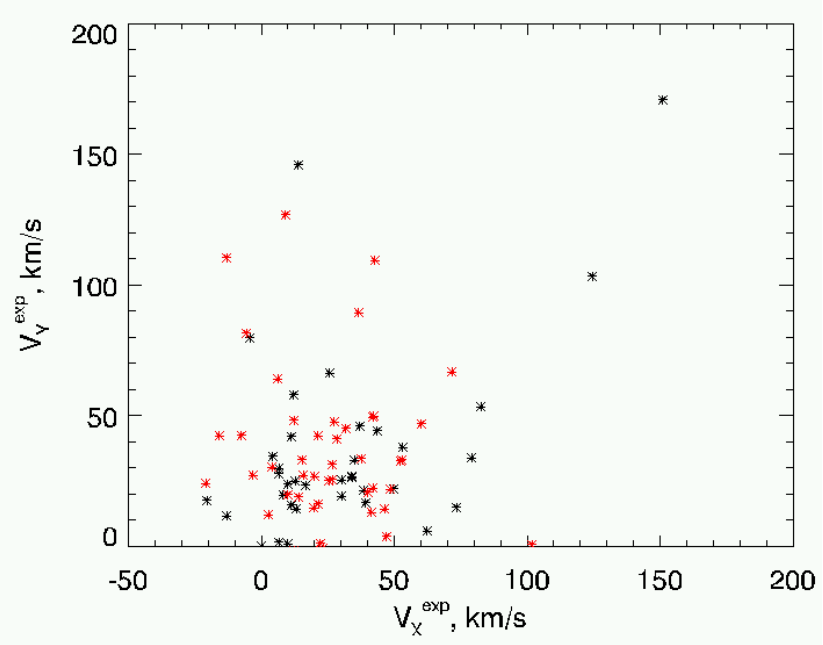

Figure 4.8: The dependence of the MC expansion velocity in the direction orthogonal to the X_{GSE} axis and the MC axis (vertical) on the X_{GSE} component of the expansion velocity, V_X^{exp} that was calculated from the linear fit of the velocity. The orthogonal expansion velocity V_Y^{exp} was calculated as the maximum value of a projection of the observed velocity onto the orthogonal axis. We separated all data into two groups: black with a semi-axis ratio less than 1.4 and red with this semi-axis ratio greater than 1.4.

4.3 Change of the ICME cross-section

Russell and Mulligan (2002) presented a gas-dynamic estimation of the distance of an ICME driven shock to the ICME as the obstacle. The examples of such shocks are shown in Figures 4.9 and 4.10. For usual solar wind Mach numbers, this distance equals about 0.2 of the obstacle radius, while several observations made by the Pioneer Venus spacecraft provide a relation between this distance and half-thickness of the MC about 0.6. One of the explanation is that the real radius of curvature of the MC is larger than the half thickness of the MC that is usually considered as a radius in one-point observation. As we already noted, this led to presumption of oblate shapes of ICMEs.

To analyze the ICME deformation, we estimated the thickness of ICME-sheath using the times of its observations and the average plasma velocity of plasma within it and the radius of the MC obtained with the force-free flux rope model fitting by *Lynnyk and Vandas* (2009). We compared it with the radius of the MC curvature calculated according to the *Russell and Mulligan* (2002) equation

$$\frac{\Delta}{R_C} = 0.195 + \frac{0.78}{{M_a}^2 - 1} \tag{4.21}$$

where Δ is the MC-sheath thickness, R_C is a radius of curvature of the obstacle, and M_a is the Alfvén Mach number. We performed a study of ratios of the MC curvature radius computed from Equation 4.21 to its observed radius, Rc/R, to find the sources that affect this ratio. The results are shown in Figure 4.12, where the dependence of Rc/R is plotted as a function of the Alfvén Mach number and the magnetic field strength inside of the MC. The R_c/R ratios increase with M_A and decrease with an increasing relative inner magnetic field. The relative inner magnetic field is the ratio of the axial magnetic field from the fit (*Lynnyk and Vandas*, 2009) to the magnetic field in the ambient solar wind. We suggest that a fast moving MC is deformed due to the solar wind drag force. On the other hand, if the inner magnetic field is high, it can help to keep a circular MC shape.

While the form and inner structure of MCs are well studied (*Liu et al.*, 2008), the other ICMEs are still less described (*Démoulin*, 2010), mainly because non-MC ICMEs do not exhibit the flux-rope structure and cannot be fitted by the same way as MCs. However, there is a possibility to study the form of ICMEs based on their sheath thickness because a validity of Equation 4.21 is not limited to MCs only. The thickness of the sheath depends on the velocity of the ICME (*Siscoe and Odstrcil*, 2008) and its geometry. Thus, we performed the common study of ICME- and MC-sheaths to determine the possible deformation of ICMEs/MCs during their propagation from the Sun.

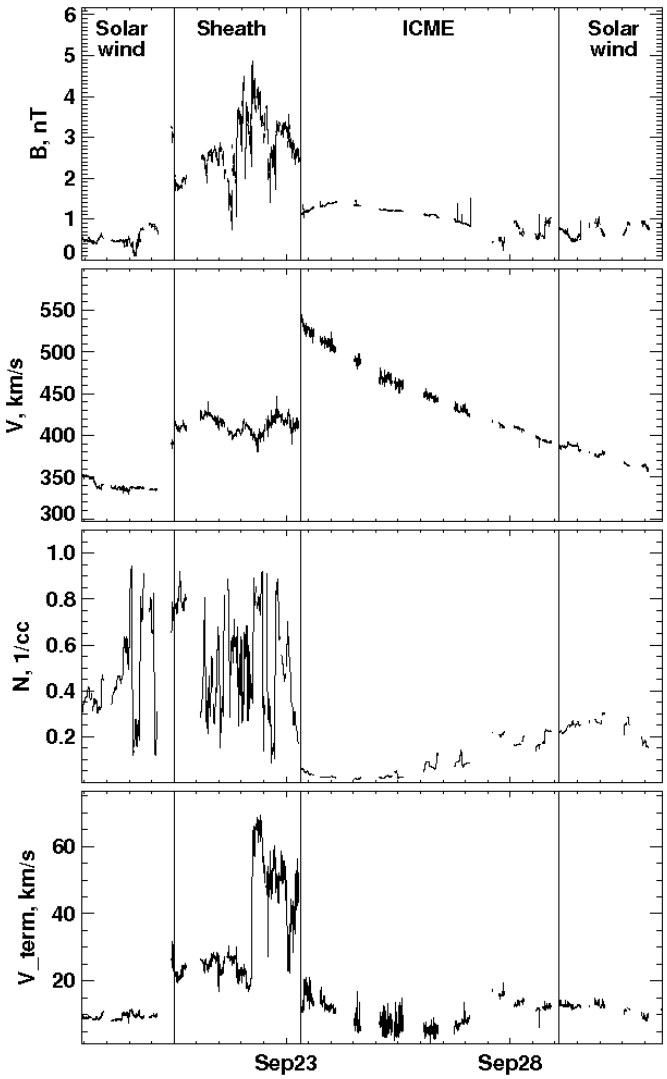

Figure 4.9: An example of the ICME identification. The event was observed by Voyager at ≈ 3.9 AU between September, 19 and October 1, 1978. The vertical lines mark the ICME and its boundaries. From top to bottom: the magnetic field strength, speed, density, and thermal velocity.

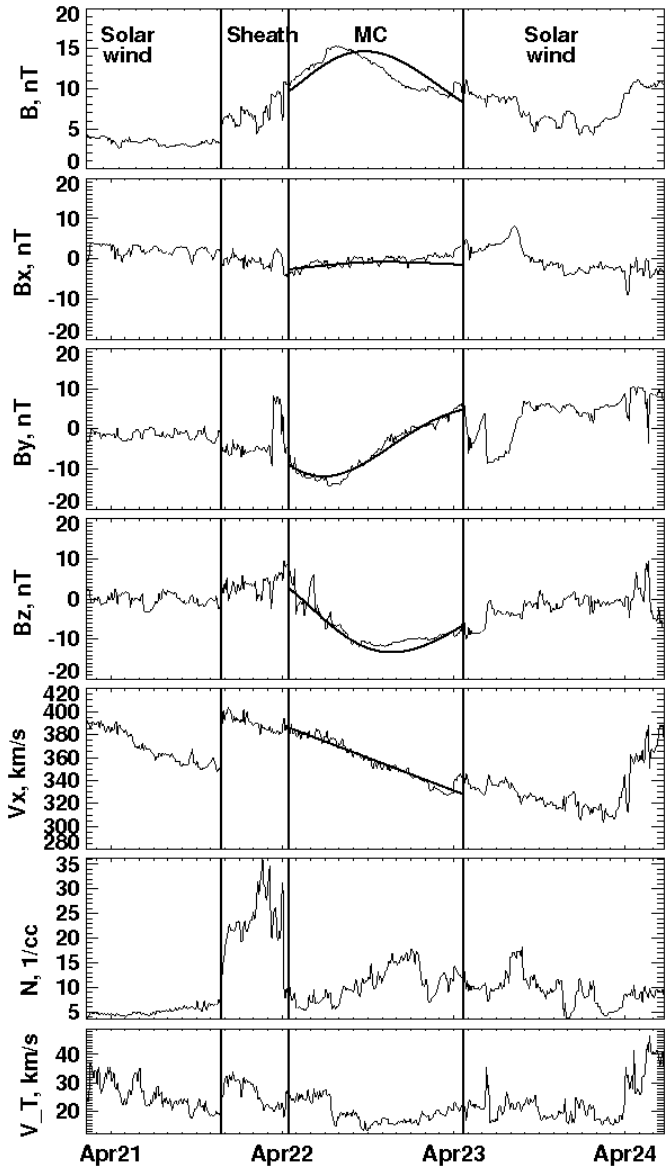

Figure 4.10: An example of the MC observation. The event was recorded by Wind from April 21 to April 24, 2001. The black lines show the results of the fits according to the *Lynnyk and Vandas* (2010) model. From top to bottom: the magnetic field strength, three components in the GSE coordinate system, Vx_{GSE} component of the velocity, proton density, and thermal speed. Different regions of the MC observation are identified and marked in the top part of the figure.

4.3.1 Deformation of the ICME cross-section

One-point measurements provide only limited information on the ICME structure and thus our analysis is based on several assumptions. Figure 4.11 shows a sketch of a flux rope with field lines connected to the Sun on both sides which reflects our current understanding of ICMEs (*Russell and Mulligan*, 2002, and references therein). To estimate the curvature of the leading edge of the flux rope, we define two curvature radii – R_1 is the bending of the flux rope, and R_2 corresponds to the flux rope cross-section (*Lynnyk et al.*, 2011). If the leading edge of the ICME expands with a supersonic velocity, a shock is formed in front of it. The distance between the ICME nose and shock, Δ, is given by *Russell and Mulligan* (2002) as:

$$\Delta = R_{obst}\,[0.195 + 0.78(M^2 - 1)^{-1}] \tag{4.22}$$

where M is the Mach number and R_{obst} is the geometric mean of R_1 and R_2. The spacecraft crossing of an ICME provides a time series of plasma parameters and magnetic field as it shown in Figure 4.9. In such plots, the shock and ICME edges can be identified and the time differences can serve as a proxy for the ICME spatial dimensions under the assumption that the whole structure propagates with the speed measured inside the ICME. We denote the length of the spacecraft path through the ICME as $2R$ and the distance between the ICME leading edge and the shock as D. The distance, D will be used as the sheath thickness but it is clear that D is an upper limit to the real thickness of the sheath at the ICME nose (see Figure 4.11 for explanation). Since the ICME cross-section is unknown, we assume a circular shape with radius R.

The apparent radius of curvature, R_C is determined from the equation

$$R_C = D\,\frac{1}{[0.195 + 0.78(M^2 - 1)^{-1}]}. \tag{4.23}$$

These simplifications are very crude but one-point measurements generally provide limited constraints. Nevertheless, the procedure was applied for both the ICMEs and MCs.

We used the list of ICMEs observed by Voyager 2 between 1 and 30 AU (*Wang and Richardson*, 2004) and the list of magnetic clouds observed by Wind (*Lepping et al.*, 2006). We selected the events with clear shocks in front of the ICMEs/MCs. We obtained 23 MCs and 26 ICMEs (from the MCs and 168 ICMEs listed). We visually inspected magnetic field and plasma parameters and determined the edges of ICMEs/MCs which correspond to sharp changes of these parameters. The same procedure was applied for the selection of shocks. We should note that our identification of MC edges corresponds perfectly with the boundaries of *Lepping et al.* (2006), whereas we slightly corrected several estimations of the ICME edges made by *Wang and Richardson* (2004). Examples of our identifications of the boundaries can be found in Figures 4.9 and 4.10.

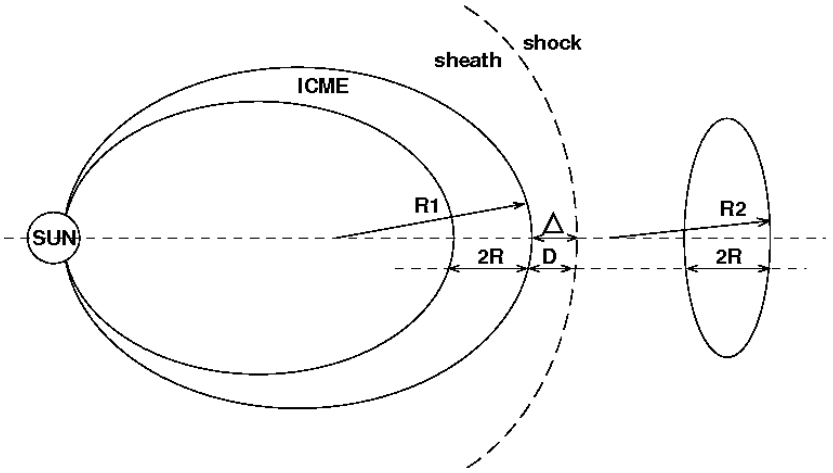

Figure 4.11: A schematic illustration of the ICME geometry and definition of its parameters. A view of the side (left) and the ICME cross-section in the plane perpendicular to the left part (right). $R1$ – the curvature radius at the ICME nose; $R2$ – the curvature radius that corresponds to the ICME cross-section; $2R$ - the ICME dimension seen by a spacecraft; Δ - the sheath thickness at the ICME nose; and D - the sheath thickness observed by a spacecraft.

For each of the selected events, we determined the sheath thickness, D, under the aforementioned assumptions and the apparent radius of curvature, R_C, was calculated according to Equation 4.23 where we use the Alfvén Mach number for M.

Figure 4.12a shows the R_C/R ratio as a function of the Alfvén Mach number of the leading edge of the ICMEs that do not exhibit MC structure. The ratio generally exceeds unity, the apparent radius, R_C, calculated from the magnetosheath thickness is larger than the radius of the ICME cross-section. Taking into account the method of determination of these quantities shown in Figure 4.11, one can see that R represents lower and R_C upper estimates of the real ICME/MC cross-sections. On the other hand, Figure 4.12b show that if the Mach number is small enough, the R_C/R ratio can be be smaller than unity. We have checked three MCs denoted by diamonds in Figure 4.12b and found that the expansion effect dominates in these cases and the sheath is created by a different mechanism.

The R_C/R ratio increases with increasing Mach number in both panels of Figure 4.12. This trend is reliably determined in Figure 4.12b where the data for MCs are plotted (the points denoted as diamonds were excluded from the fit). We believe that the increase of the R_C/R ratio with the Mach number is caused by the deformation of the ICME/MC cross-sections. The deformation of low-Mach number ICMEs/MCs is small and thus their cross-sections are nearly circular. As a result, the R_C calculated from the sheath thickness becomes close to R obtained from the duration of the ICME/MC. On the other hand, the fast ICME with high Mach number is largely deformed through interaction with the

ambient solar wind and the R_C/R ratio increases (see Figure 4.11).

Since the structure of ICMEs, and especially MCs, is maintained by the internal magnetic field, we plotted the R_C/R ratio as a function of the ratio of the peak magnetic field strength inside the ICME/MC to the surrounding IMF in Figures. 4.13a (ICMEs) and 4.13b (MCs). These figures show that large R_C/R ratios are not observed for ICMEs/MCs with a strong internal magnetic field. This result supports our hypothesis that the high internal magnetic field keeps the ICME/MC shape close to the circular cross-section. This trend is more distinct in the MC subset in Figure 4.13b than in the ICME data set, but it is not clear, whether this difference is due to fact that the MC observations were made at 1 AU and the ICMEs (Figure 4.13a) were observed along the trajectory of Voyager 2 from 1 to 30 AU. Note that the ratios of R_C/R for ICMEs are often larger than those for MCs (see vertical axes in Figure 4.13), whereas the ratios of magnetic fields B_{ICME}/B_{SW} (horizontal axes) generally exceed the B_{MC}/B_{SW} ratios.

Voyager 1 and 2 observations of the IMF from 1 AU to the termination shock revealed that the mean IMF strength decreases with heliospheric distance, L, as $1/L$. The mean IMF strength drops by a factor of 30 from 1 to 30 AU. Enhanced ratios of B_{ICME}/B_{SW} with respect to B_{MC}/B_{SW} suggest that the B_{ICME} decreases more slowly and that the currents maintaining the B_{ICME} are still active at large distances from the Sun. We plot the R_C/R ratios of the ICMEs and MCs as a function of a heliospheric distance, L in Figure 4.14. The figure suggests that the ICME shapes deform during the propagation through interplanetary space (*Lynnyk et al.*, 2011). The spread of the experimental points is largely due to simplifications made in calculations of both R_C and R but the linear fit shown in the figure reveals an increasing trend of their ratios with distance from the Sun. This increase can be interpreted as the increasing oblateness of the ICMEs.

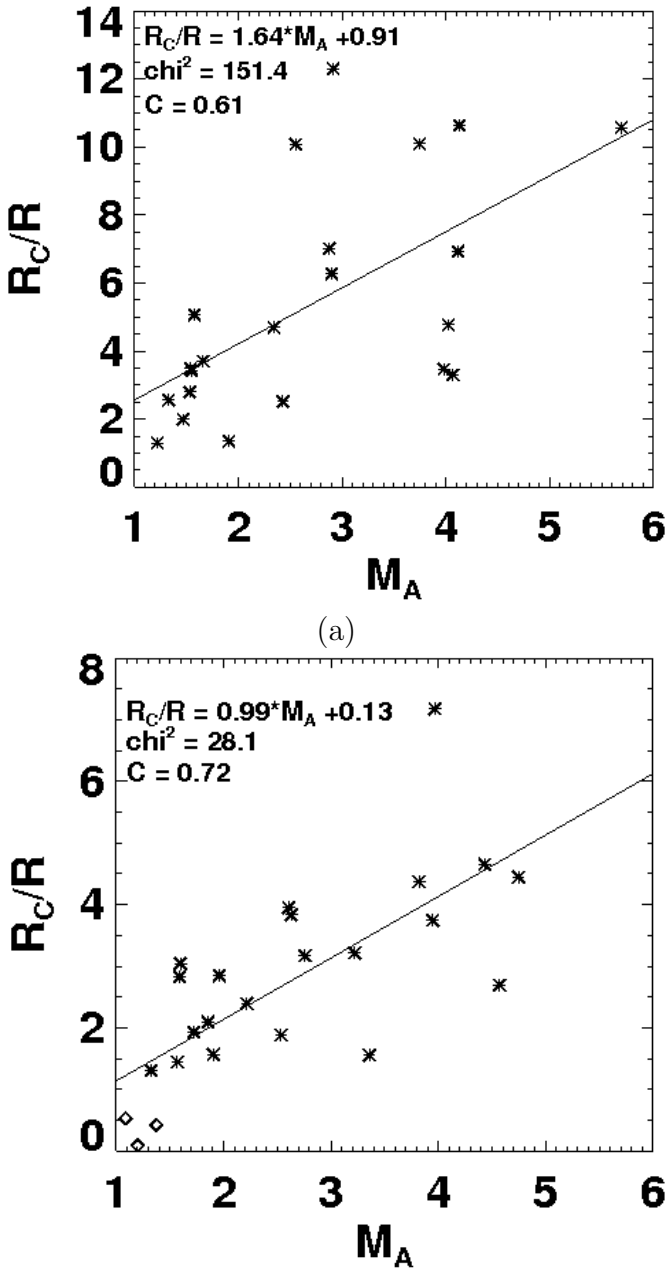

Figure 4.12: The R_C/R ratios of ICMEs (a) and MCs (b) as a function of the Alfvén Mach number. The set of ICMEs does not include MCs. The lines represent linear fits to the points. Fit parameters are given inside the panels (C represents the correlation coefficient of the fit).

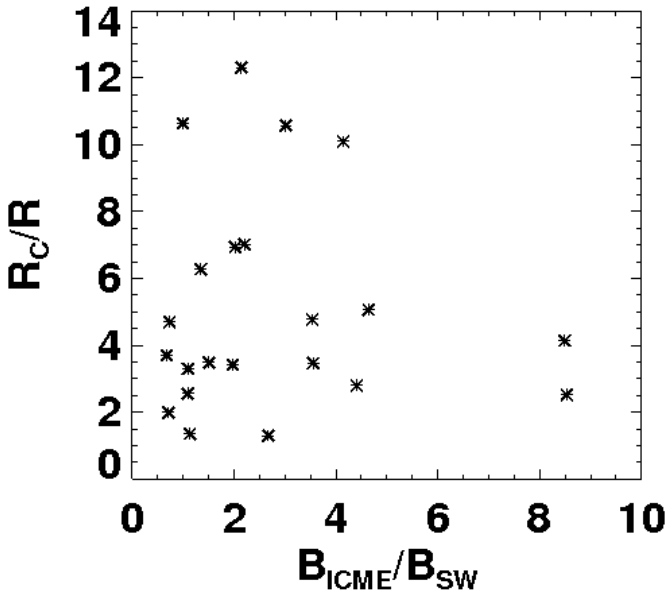

(a)

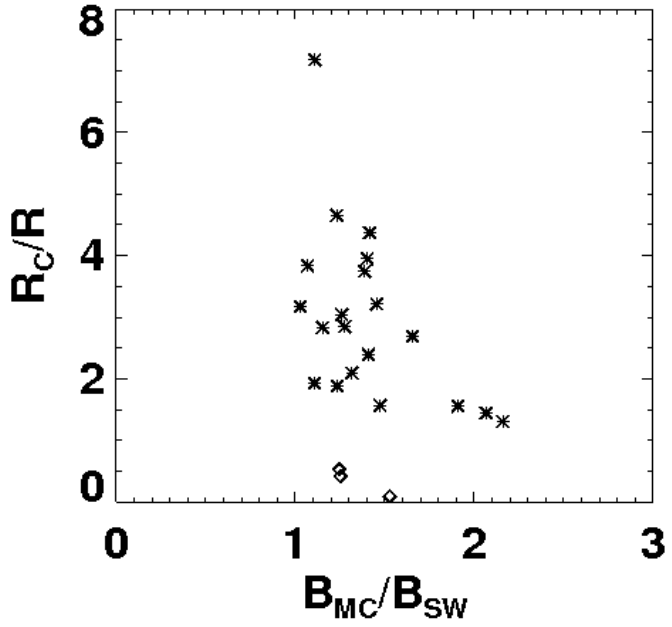

(b)

Figure 4.13: The R_C/R ratios of ICMEs (a) and MCs (b) as a function of the peak magnetic field strength inside the ICME/MC normalized to the ambient IMF (marked as B_{SW}).

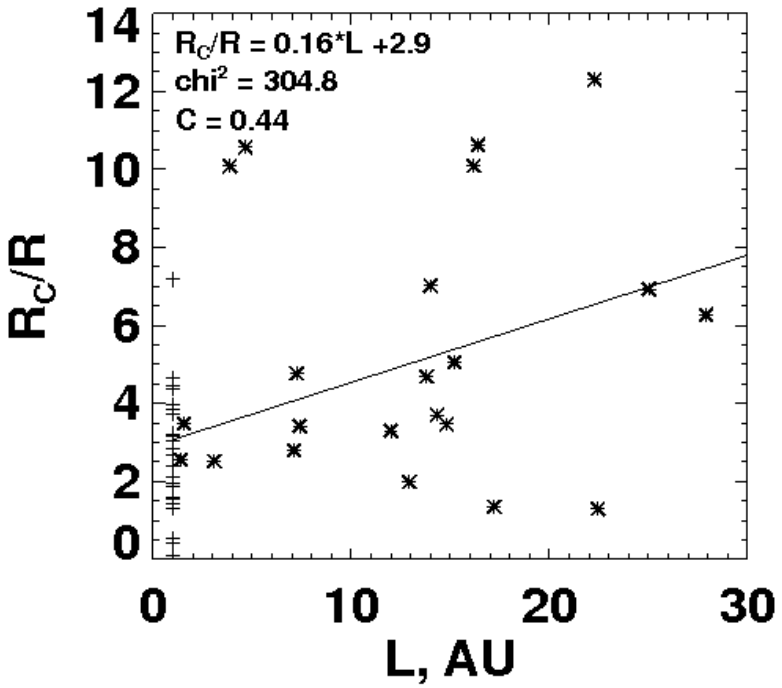

Figure 4.14: The R_C/R ratio of ICMEs (observed by Voyager 2 and marked by stars) and MCs (observed by WIND and marked by crosses) as a function of a heliospheric distance, L. The line represents the best fit to the points. Fit parameters are given inside the panel.

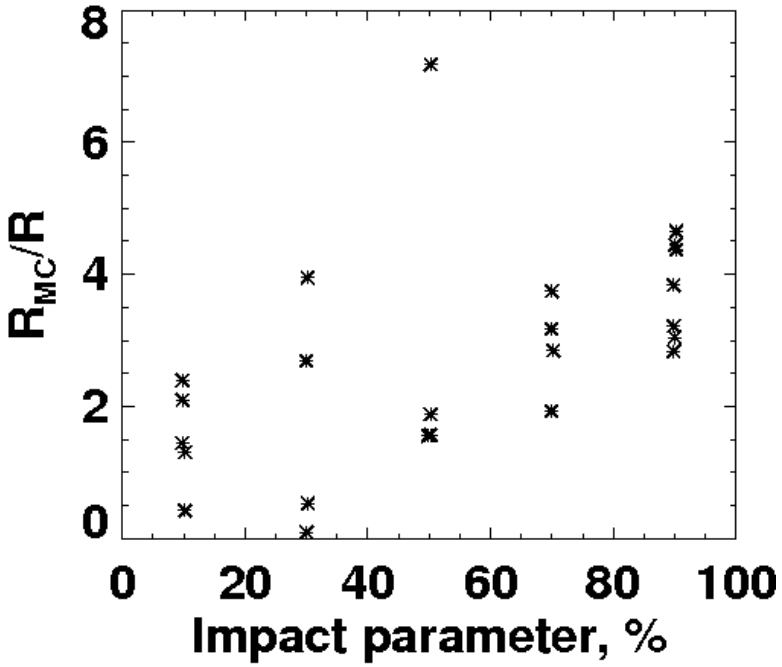

Figure 4.15: The R_{MC}/R ratio of MCs as a function of the impact parameter.

4.3.2 Deformation of the MC cross-section

In the previous section, R is determined under an assumption that the spacecraft crosses near the ICME/MC axis. This assumption is probably a source of large errors in the R determination. Such an effect can be inferred from Figure 4.15 where the R_C/R ratio is plotted as a function of the impact parameter. These two quantities should be independent, but Figure 8 shows that the R_C/R ratio increases when the impact parameter becomes large. The large impact parameter means that the spacecraft crosses the MC far away from its axis.

However, if the observed event exhibits MC features, the fit of observed parameters can provide a deeper insight into its spatial structure. For this reason, we have applied the flux rope model (the *Lynnyk and Vandas* (2010) approach) to the MC subset. The model assumes a cylindrical expanding flux rope with a circular cross-section. The fit of the data provides the flux rope radius R_{MC} and the impact parameter (i.e., the distance of the spacecraft trajectory from the MC center relative to R_{MC}). Note that for expanding MCs these values describe a particular MC at the moment of observation of its leading edge. Figure 4.10 shows an example of a fit to one MC. The good agreement of the fits with the measured data suggests that the model assumptions are reasonable. An application of R_{MC} and the impact parameter from the fit significantly decreases the uncertainty in the determination of the MC cross-sections. We use the impact parameter to correct the sheath thickness assuming that the shock can be approximated by a circle near the obstacle nose as depicted in Figure 4.16. In such a case, the apparent radius of curvature is computed from the magnetosheath thickness according to:

$$R_C = \Delta \frac{1}{[0.195 + 0.78(M^2 - 1)^{-1}]} \tag{4.24}$$

For the circular MC R_C is equal to the R_{MC} and Δ is equal to the Δ_{MC}.

In order to account for this effect, we have made a model fitting (using the model of the non-expanding flux rope) to the MC set analyzed in the previous section and obtained R_{MC} and the impact parameter as it is shown in Figure 4.16. The R_C/R_{MC} ratio is calculated from the MC radius (R_{MC}) obtained by the fit and from the apparent MC radius, R_C determined from the sheath thickness, Δ, that was corrected by the impact parameter.

Figure 4.17 a is a counterpart of Figure 4.12b; it shows the R_C/R_{MC} ratio as a function of the Alfvénic Mach number, M_A. One can note that the corrections change the figure substantially. The R_C/R_{MC} ratios in Figure 4.17 a reach generally lower values than the corresponding R_C/R ratios in Figure 4.12b except for two points (marked as triangles in Figure 4.17) that keep the large R_C/R_{MC} values. We revisited these two observations and found complicated situations in both cases. We have identified two MCs following one another with a temporal separation of about 20 hours, i.e., with separations similar to the durations of

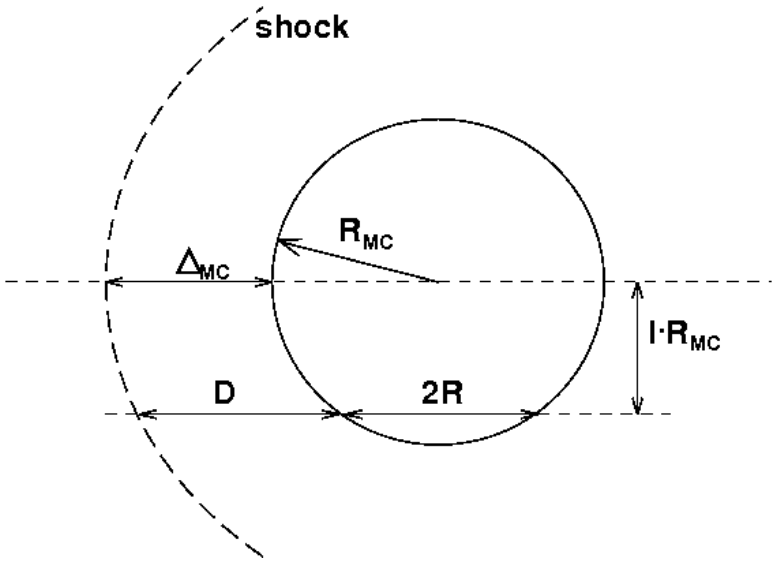

Figure 4.16: A sketch of the MC cross-section. A cylindric MC with radius, R_{MC} pushes a shock (dashed) separated by the sheath thickness, Δ_{MC}. The spacecraft crosses the structure at the distance $I \cdot R_{MC}$ from its axis (I is the impact parameter) and observes the sheath thickness, D and the MC dimension, $2R$.

observations of each of them. We suggest that a joint bow shock was created in front of this MC pair. Consequently, the radius of this combined structure would be a factor of ≈ 3 larger than the radius of the first MC that results from the fit and that was used for R_C/R_{MC} calculation. The linear trend shown in Figure 4.12a does not include these two points. Its slope is not so steep as that in Figure 4.12b but the trend of an increase of the R_C/R_{MC} ratio with M_A persists.

We expected that using the fits of MCs for more accurate determination of the deformation of the MC cross-section will improve the dependence of the deformation of the MCs on the Mach number. Comparing the results of two methods used to determine the MC geometry, we note that the using the fits of MCs do not bring the expected effect. The corrections resulting from the fits decreased large values of R_C/R (Figure 4.12b) to more reasonable values R_C/R_{MC} (Figure 4.17a), however, this correction decreases the small values (denoted by diamonds) as well. Such small values would suggest a bullet-like shape of the MC cross-section that is hardly probable and thus we should find other effects to provide an explanation of these thin sheaths.

Our estimates of R_C are based on the *Russell and Mulligan* (2002) approach that is valid for a non-expanding flux rope that propagates through the ambient solar wind with a supersonic speed. However, *Siscoe and Odstrcil* (2008) show that the sheath would be thinner if a flux rope was at rest in the solar wind frame but expanding with a supersonic speed. The velocity profiles measured inside the analyzed events suggest that expansion is important in most of them.

Figure 4.18 shows an example of such MC. The locations of the bow shock and MC edges are distinguished by the vertical lines. The velocity inside a MC decreases linearly and it can be interpreted as the MC expansion with a speed of 33.3 km/s. On the other hand, the MC propagation speed (344 km/s) is very close to the solar wind speed in front of the shock (349 km/s). It means that the center of this particular MC is nearly at the rest in the solar wind frame and that the low-Mach number shock ($M_A \approx 1.2$) leading the ICME is created by the MC expansion. Note that similar parameters were identified for all three events denoted by the diamonds in Figure 4.17a.

The R_C/R_{MC} ratios fluctuate generally between 1 and 2 if the points denoted by triangles and diamonds are excluded, however, the R/R_C ratios in Figure 4.12b reach the value of 4. It means that the typical MC cross-section would be closer to circular than Figure 4.12a suggests. The same probably hold for ICMEs in Figure 4.12b but this hypothesis cannot be confirmed by corresponding fit. We believe that the results in Figure 4.17a are more reliable because the determination of the MC diameter uses the whole magnetic field profile and the sheath thickness as well as the MC diameter are corrected by the impact parameter.

For completeness, Figure 4.17b shows the ratio R_C/R_{MC} as a function of the ratio of the magnetic field at the MC center (from the fit) to the ambient magnetic field. This figure can be considered as a correction of Figure 4.13b. We can see that if the ratio of magnetic fields B_{fit}/B_{SW} is two or larger, the R_C/R_{MC} ratio is close to unity and the cross-section of such MC is nearly circular. This result supports our suggestion that the axial current creating the magnetic field inside the MC helps to keep its cylindrical form (*Lynnyk et al.*, 2011).

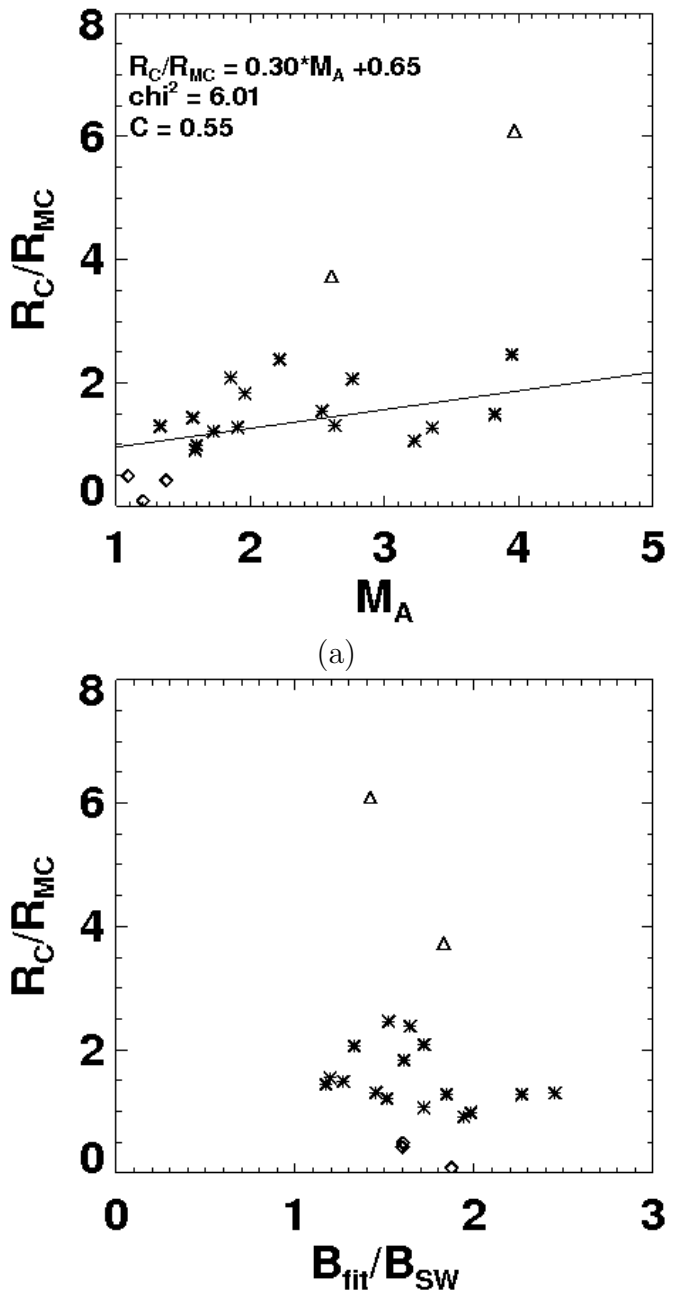

(a)

(b)

Figure 4.17: The R_C/R_{MC} ratio as a function of the (a) Alfvén Mach number and the (b) magnetic field strength at the MC axis normalized to the ambient IMF. The full line represents the fit with parameters inside the panel.

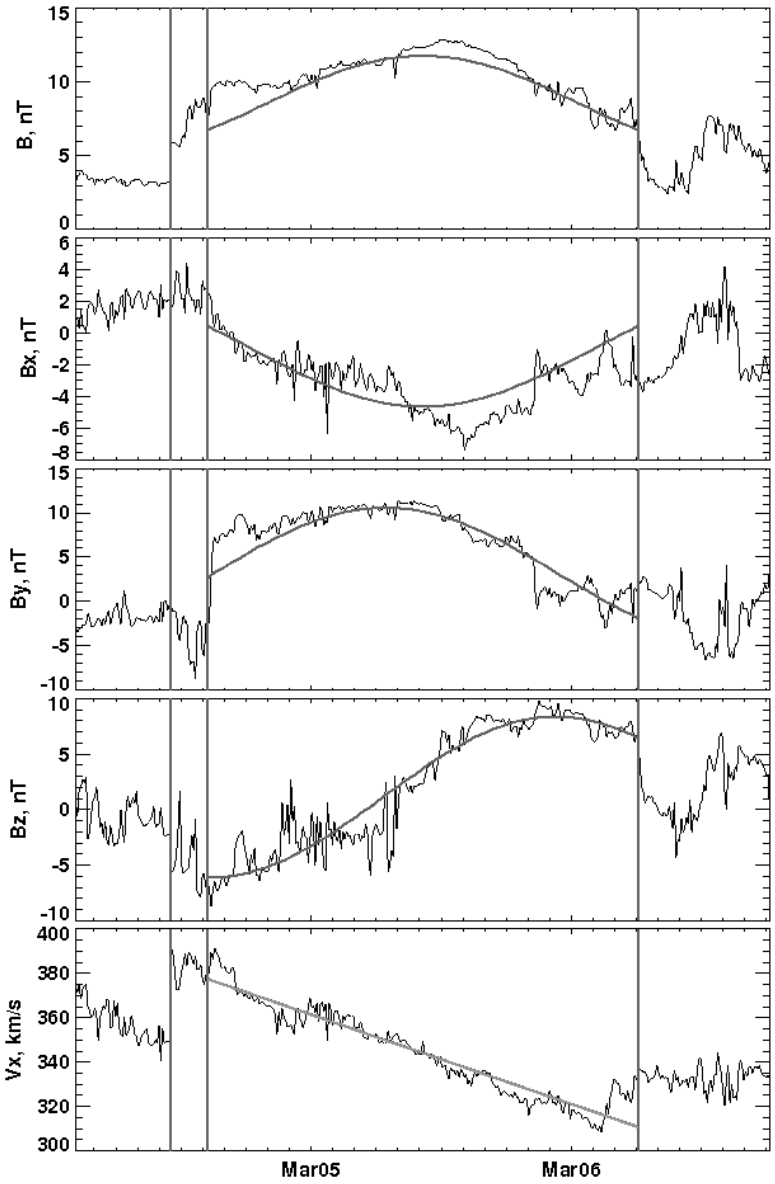

Figure 4.18: An example of the thin sheath of MC observation by Wind from March 4 to March 6, 1998. From top to bottom: the magnetic field strength, and three components in the GSE coordinate system, and the $-Vx_{GSE}$ component of the velocity. The black lines show the fits of parameters according to the *Lynnyk and Vandas* (2010) model. Specification of observation: the expansion velocity - 33.3 km/s, the mean velocity within the MC - 344 km/s, the solar wind velocity prior to the shock - 349 km/s, the MC leading edge velocity - 385 km/s, and the Alfvén Mach number - 1.16.

4.4 MC boundary distortion

As it was noted in the section 1.5, the MC cross-section may be deformed due to distribution of the SW velocity. We suppose that the MC cross-section may be distorted on a small scale like Figure 4.19 shows. For the evaluation of this distortion we compare the direction of the normals to the boundary estimated by different ways. The MC boundary may be taken as a tangential discontinuity in the magnetic field or as a surface that separates the solar wind and the MC. We used again MCs from the *Lepping et al.* (2006) list to find those that have a clear visible discontinuity og the magnetic field at their leading edge. As the discontinuity, we consider that which have at least one component changing more than for 2 nT at the boundary. We assume that the MC boundary is the tangential discontinuity, thus we calculated boundary normal as a vector product of the magnetic field vectors taken at both sides of the boundary (see Figure 4.7). We calculated the MC axis direction using the elliptical model fit and we obtained the direction of the boundary normal for the elliptical flux rope. We compared this modeled normal with that obtained from the magnetic configuration of the boundary. In Figure 4.19, an illustration of the projections of the normals to the plane perpendicular to the MC axis is shown. The distribution of this angle is shown in Figure 4.20. One can see that this angle can reach values from 0 to 90 degrees with the most probable values in a range from 20 to 90 degrees.

As a confirmation of the reasonable values for the normal calculated through the magnetic configuration of the boundary, we made the comparison of this normal with the MC axis (see Figure 4.21). As it can be seen from Figure 4.22, this normal is usually almost perpendicular to the MC axis. This means that the MC boundary is almost non-deformed in the plane of the MC axis, whereas its cross-section is probably strongly distorted (Figure 4.20).

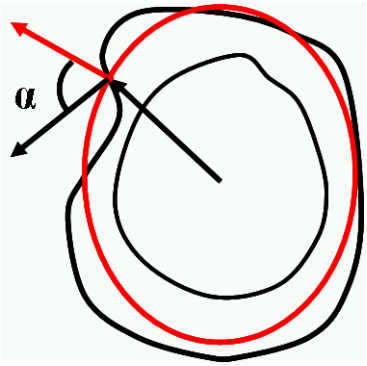

Figure 4.19: An illustration of the possible distortion of the MC boundary (thick black curve) from the MC boundary modeled using the magnetic field fit (red circle) in a plane perpendicular to the MC axis. The boundary normal calculated from the magnetic field orientation on the boundary (black arrow) and the boundary normal expecting a cylindrical MC (red arrow) are shown. α indicates the angle between these two normals.

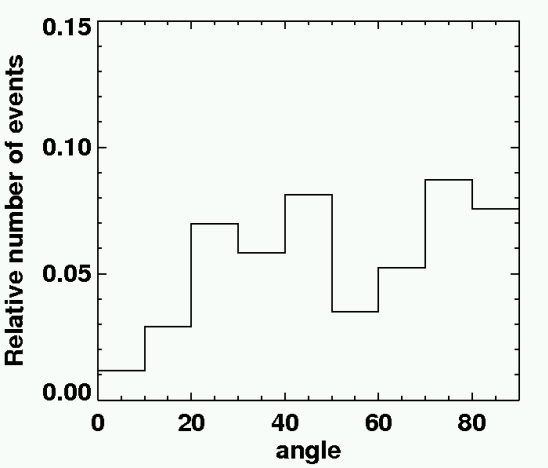

Figure 4.20: The distribution of the angle (marked as α in Figure 4.19.) between the MC boundary normals calculated through the fit and through magnetic configuration of the boundary.

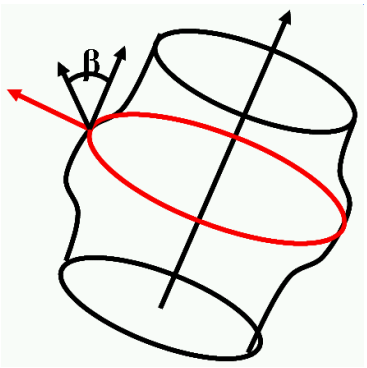

Figure 4.21: An illustration of the possible distortion of the MC boundary (thick black curve). The red circle indicates the cross-section of the MC modeled by the magnetic field fit. The boundary normal calculated from the magnetic field orientation on the boundary (black arrow) and the boundary normal expecting an elliptical MC (red arrow) are shown. β indicates the angle between normal calculated with the boundary magnetic orientation and MC axis.

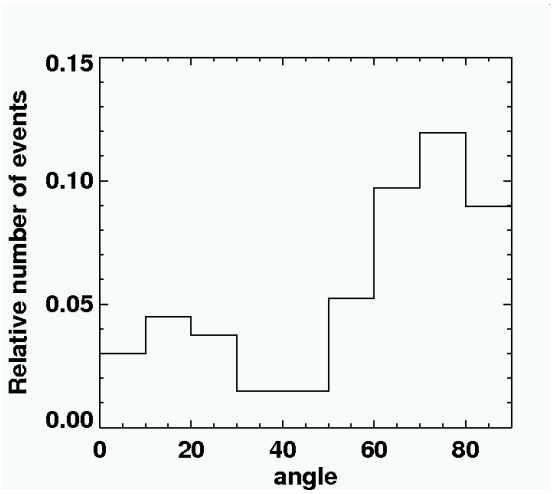

Figure 4.22: The distribution of the angle (marked as β in Figure 4.21.) between MC axis and the MCs boundary normal calculated through the magnetic configuration of the boundary.

Chapter 5

Conclusions

This work is devoted to the study of the deformation of ICMEs. There are several manifestations of the deformation of ICMEs at the Earth orbit: the velocity gradient within ICME boundaries that indicates the expansion of the ICME; the mismatch between the stand-off distance of the shock observed in front of supersonical ICMEs and that expected for the cylindrical structure, it is an indication of the oblateness of ICMEs; internal magnetic field profiles that are unexplained by the cylindrical models of MCs.

In *Lynnyk and Vandas* (2009) we modified equations of the cylindrical force-free model by expansion parameters obtained from the velocity profile. We have shown that the expansion is observed in 85% of MCs and that this expansion strongly affects their magnetic field structure (*Lynnyk and Vandas*, 2010). We obtained the different dependences for the MCs observed close to their axes and for those that were observed far from it. This can be explained by larger disturbances in the outer regions of the MC. We confirmed that the expansion model provides better fits in 70% of investigated MCs.

We performed the study of MC cross-sections using the force-free model modified to the elliptical MCs. From results it follows that the MCs are slightly deformed into the oblate cross-section. However, it is shown that the elliptical model should be used together with the other features that indicate an oblate shape of MCs.

We present a statistical analysis of the ICME/MC deformation based on the thickness of sheaths observed in front of them. According to *Lynnyk et al.* (2011), we can conclude that:

1. The shock and sheath are always present in front of ICMEs/MCs if their leading edge propagates with a supersonic speed.

2. If the supersonic propagation is caused by the ICME/MC expansion, the sheath is thinner than that caused by the supersonic propagation of the whole flux rope, consistent with the suggestion of *Siscoe and Odstrcil* (2008).

3. The apparent radius of curvature calculated from the sheath thickness slightly increases with the Mach number. This effect was attributed to the larger deformation of the fast ICME/MC.

4. The apparent radius of the ICME curvature (and deformation) increases with the heliospheric distance.

5. If the magnetic field inside the ICME/MC is much stronger than that in the ambient solar wind, the ICME/MC cross-section is closer to circular.

6. The ratio of magnetic fields inside and around the ICME is larger at larger distances from the Earth. It suggests a principal contribution of the current inside the ICME to its internal field.

For a subset of ICMEs that exhibit the MC structure, we performed the additional analysis that helped us to avoid the overestimation of the MC deformation.

We have shown that, in spite of several limitations of one-point observations, investigations of ICME/MC sheaths can contribute to our understanding of the geometry and evolution of flux ropes in the solar wind.

We performed the analysis of the MC boundaries and found evidence of the distortion of MCs in the plane perpendicular to their radius.

References

Antiochos, S. K., C. R. DeVore, and J. A. Klimchuk (1999), A Model for Solar Coronal Mass Ejections, *Astrophys. J.*, *510*, 485–493, doi:10.1086/306563. 5

Behannon, K. W., M. H. Acuna, L. F. Burlaga, R. P. Lepping, N. F. Ness, and F. M. Neubauer (1977), Magnetic field experiment for Voyagers 1 and 2, *Space Sci. Rev.*, *21*, 235–257, doi:10.1007/BF00211541. 24

Bothmer, V., and R. Schwenn (1998), The structure and origin of magnetic clouds in the solar wind, *Ann. Geophys*, *16*, 1–24, doi:10.1007/s00585-997-0001-x. 13

Bothmer, V., et al. (1996), Energetic particles and coronal mass ejections in the high latitude heliosphere: Ulysses-LET observations, in *American Institute of Physics Conference Series*, *American Institute of Physics Conference Series*, vol. 382, edited by D. Winterhalter, J. T. Gosling, S. R. Habbal, W. S. Kurth, & M. Neugebauer, pp. 445–448, doi:10.1063/1.51495. 14

Bridge, H. S., J. W. Belcher, R. J. Butler, A. J. Lazarus, A. M. Mavretic, J. D. Sullivan, G. L. Siscoe, and V. M. Vasyliunas (1977), The plasma experiment on the 1977 Voyager mission, *Space Sci. Rev.*, *21*, 259–287, doi:10.1007/BF00211542. 24

Brueckner, G. E., et al. (1995), The Large Angle Spectroscopic Coronagraph (LASCO), *Sol. Phys.*, *162*, 357–402, doi:10.1007/BF00733434. 4

Burlaga, L., E. Sittler, F. Mariani, and R. Schwenn (1981), Magnetic loop behind an interplanetary shock - Voyager, Helios, and IMP 8 observations, *J. Geophys. Res.*, *86*, 6673–6684, doi:10.1029/JA086iA08p06673. 8

Burlaga, L. F. (1988), Magnetic clouds and force-free fields with constant alpha, *J. Geophys. Res.*, *93*, 7217–7224, doi:10.1029/JA093iA07p07217. 25

Burlaga, L. F., R. P. Lepping, and J. A. Jones (1990), Global configuration of a magnetic cloud, in *Physics of Magnetic Flux Ropes. AGU, Washington, DC*, edited by Russell, E. R., Priest, C. T., Lee, L. C., pp. 373–377. 13, 27

Byrne, J. P., P. T. Gallagher, R. T. J. McAteer, and C. A. Young (2009), The kinematics of coronal mass ejections using multiscale methods, *Astronomy and Astrophysics*, *495*, 325–334, doi:10.1051/0004-6361:200809811. 5, 7

REFERENCES

Cargill, P. J. (2004), On the Aerodynamic Drag Force Acting on Interplanetary Coronal Mass Ejections, *Sol. Phys.*, *221*, 135–149, doi:10.1023/B:SOLA.0000033366.10725.a2. 7

Chen, J. (1989), Effects of toroidal forces in current loops embedded in a background plasma, *Astrophys. J.*, *338*, 453–470, doi:10.1086/167211. 6

Chen, J. (1996), Theory of prominence eruption and propagation: Interplanetary consequences, *J. Geophys. Res.*, *101*, 27,499–27,520, doi:10.1029/96JA02644. 5

Cid, C., M. A. Hidalgo, T. Nieves-Chinchilla, J. Sequeiros, and A. F. Viñas (2002), Plasma and Magnetic Field Inside Magnetic Clouds: a Global Study, *Sol. Phys.*, *207*, 187–198. 9, 11

Dasso, S., C. H. Mandrini, P. Démoulin, and M. L. Luoni (2006), A new model-independent method to compute magnetic helicity in magnetic clouds, *Astronomy and Astrophysics*, *455*, 349–359, doi:10.1051/0004-6361:20064806. 9, 12

Démoulin, P. (2010), Interaction of ICMEs with the Solar Wind, in *American Institute of Physics Conference Series*, *American Institute of Physics Conference Series*, vol. 1216, edited by M. Maksimovic, K. Issautier, N. Meyer-Vernet, M. Moncuquet, & F. Pantellini, pp. 329–334, doi:10.1063/1.3395866. 8, 40

Démoulin, P., and S. Dasso (2009), Causes and consequences of magnetic cloud expansion, *Astronomy and Astrophysics*, *498*, 551–566, doi:10.1051/0004-6361/200810971. 13

Ebert, R. W., D. J. McComas, H. A. Elliott, R. J. Forsyth, and J. T. Gosling (2009), Bulk properties of the slow and fast solar wind and interplanetary coronal mass ejections measured by Ulysses: Three polar orbits of observations, *J. Geophys. Res. (Space Phys.)*, *114*, 1109–+, doi:10.1029/2008JA013631. 7

Farrugia, C. J., L. F. Burlaga, V. A. Osherovich, I. G. Richardson, M. P. Freeman, R. P. Lepping, and A. J. Lazarus (1993), A study of an expanding interplanatary magnetic cloud and its interaction with the earth's magnetosphere - The interplanetary aspect, *J. Geophys. Res.*, *98*, 7621–7632, doi:10.1029/92JA02349. 13, 14

Farrugia, C. J., et al. (1999), A uniform-twist magnetic flux rope in the solar wind, in *American Institute of Physics Conference Series*, *American Institute of Physics Conference Series*, vol. 471, edited by S. T. Suess, G. A. Gary, & S. F. Nerney, pp. 745–748, doi:10.1063/1.58724. 9

Forbes, T. G., and E. R. Priest (1995), Photospheric Magnetic Field Evolution and Eruptive Flares, *Astrophys. J.*, *446*, 377–+, doi:10.1086/175797. 5

Gallagher, P. T., G. R. Lawrence, and B. R. Dennis (2003), Rapid Acceleration of a Coronal Mass Ejection in the Low Corona and Implications for Propagation, *Astrophys. J. Lett.*, *588*, L53–L56, doi:10.1086/375504. 7

Gold, T., and F. Hoyle (1960), On the origin of solar flares, *Monthly Notices of the Royal Astronomical Society*, *120*, 89–+. 9, 11

Gopalswamy, N., W. T. Thompson, J. M. Davila, M. L. Kaiser, S. Yashiro, P. Mäkelä, G. Michalek, J. Bougeret, and R. A. Howard (2009), Relation Between Type II Bursts and CMEs Inferred from STEREO Observations, *Sol. Phys.*, *259*, 227–254, doi:10.1007/s11207-009-9382-1. 5

Gosling, J. T. (1990), Coronal mass ejections and magnetic flux ropes in interplanetary space, *Washington DC American Geophysical Union Geophysical Monograph Series*, *58*, 343–364. 4, 6, 14

Gosling, J. T., V. Pizzo, and S. J. Bame (1973), Anomalously low proton temperatures in the solar wind following interplanetary shock waves - evidence for magnetic bottles?, *J. Geophys. Res.*, *78*, 2001–2009, doi:10.1029/JA078i013p02001. 14

Harrison, R. A., et al. (2008), First Imaging of Coronal Mass Ejections in the Heliosphere Viewed from Outside the Sun Earth Line, *Sol. Phys.*, *247*, 171–193, doi:10.1007/s11207-007-9083-6. 4

Hidalgo, M. A., C. Cid, J. Medina, and A. F. Viñas (2000), A new model for the topology of magnetic clouds in the solar wind, *Sol. Phys.*, *194*, 165–174. 9, 11

Hundhausen, A. J. (1977), An interplanetary view of coronal holes., in *Coronal Holes and High Speed Wind Streams*, edited by J. B. Zirker, pp. 225–329. 2

Kivelson, M. G., and C. T. Russell (1995), *Introduction to Space Physics*. 2, 4

Krall, J., J. Chen, R. T. Duffin, R. A. Howard, and B. J. Thompson (2001), Erupting Solar Magnetic Flux Ropes: Theory and Observation, *Astrophys. J.*, *562*, 1045–1057, doi:10.1086/323844. 5

Larson, D. E., et al. (1997), The Solar Source of the October 18-20, 1995 Magnetic Cloud inferred from WIND Electron Observations at 1 AU, in *AAS/Solar Physics Division Meeting #28*, *Bulletin of the American Astronomical Society*, vol. 29, pp. 913–+. 14

Lepping, R. P., L. F. Burlaga, and J. A. Jones (1990), Magnetic field structure of interplanetary magnetic clouds at 1 AU, *J. Geophys. Res.*, *95*, 11,957–11,965, doi:10.1029/JA095iA08p11957. 25

Lepping, R. P., D. B. Berdichevsky, C. Wu, A. Szabo, T. Narock, F. Mariani, A. J. Lazarus, and A. J. Quivers (2006), A summary of WIND magnetic clouds for years 1995-2003: model-fitted parameters, associated errors and classifications, *Ann. Geophys*, *24*, 215–245. 7, 24, 25, 27, 28, 35, 43, 54

Lepping, R. P., et al. (1995), The Wind Magnetic Field Investigation, *Space Sci. Rev.*, *71*, 207–229, doi:10.1007/BF00751330. 23

REFERENCES

Liu, Y., J. D. Richardson, and J. W. Belcher (2005), A statistical study of the properties of interplanetary coronal mass ejections from 0.3 to 5.4 AU, *Planet. Space Sci.*, *53*, 3–17, doi:10.1016/j.pss.2004.09.023. 7

Liu, Y., J. D. Richardson, J. W. Belcher, C. Wang, Q. Hu, and J. C. Kasper (2006), Constraints on the global structure of magnetic clouds: Transverse size and curvature, *J. Geophys. Res. (Space Phys.)*, *111*, A12S03, doi:10.1029/2006JA011890. 17, 18

Liu, Y., W. B. Manchester, IV, J. C. Kasper, J. D. Richardson, and J. W. Belcher (2007), Determining the Magnetic Field Orientation of Coronal Mass Ejections from Faraday Rotation, *Astrophys. J.*, *665*, 1439–1447, doi:10.1086/520038. 12

Liu, Y., J. G. Luhmann, K. E. J. Huttunen, R. P. Lin, S. D. Bale, C. T. Russell, and A. B. Galvin (2008), Reconstruction of the 2007 May 22 Magnetic Cloud: How Much Can We Trust the Flux-Rope Geometry of CMEs?, *Astrophys. J. Lett.*, *677*, L133–L136, doi:10.1086/587839. 40

Lundquist, S. (1950), Magnetohydrostatic fields, *Ark. Fys.*, *2*, 361–365. 8, 11, 27, 28

Lynnyk, A., and M. Vandas (2009), Fitting of expanding magnetic clouds: A statistical study, *Planet. Space Sci.*, *57*, 1375–1380, doi:10.1016/j.pss.2009.06.015. 11, 27, 29, 40, 57

Lynnyk, A., and M. Vandas (2010), Influence of Magnetic Cloud Expansion on Its Fits, in *American Institute of Physics Conference Series*. 31, 32, 33, 42, 49, 53, 57

Lynnyk, A., J. Šafránková, and Z. Němeček (2010), Deformation of ICME and MC on 1-30 AU Seen by Voyager 2 and WIND, in *WDS'10 Proceedings of Contributed Papers: Part II–Physics of Plasmas and Ionized Media*, edited by J. Safrankova and J. Pavlu, pp. 128–134, Matfyzpress, Prague. 10

Lynnyk, A., J. Šafránková, Z. Němeček, and J. D. Richardson (2011), Deformation of ICMEs/MCs along their path, *Planet. Space Sci.*, *59*, 840–847, doi:10.1016/j.pss.2011.03.016. 43, 45, 51, 57

Marubashi, K., and R. P. Lepping (2007), Long-duration magnetic clouds: a comparison of analyses using torus- and cylinder-shaped flux rope models, *Ann. Geophys*, *25*, 2453–2477. 13

McComas, D. J., et al. (2000), Solar wind observations over Ulysses' first full polar orbit, *J. Geophys. Res.*, *105*, 10,419–10,434, doi:10.1029/1999JA000383. 3

Neugebauer, M., and R. Goldstein (1997), Particle and field signatures of coronal mass ejections in the solar wind, in *Coronal Mass Ejections, AGU, Washington*, American Institute of Physics Conference Series. 7

Ogilvie, K. W., et al. (1995), SWE, A Comprehensive Plasma Instrument for the Wind Spacecraft, *Space Sci. Rev.*, *71*, 55–77, doi:10.1007/BF00751326. 24

Osherovich, V. A., C. J. Farrugia, and L. F. Burlaga (1993), Dynamics of aging magnetic clouds, *Advances in Space Research*, *13*, 57–62, doi:10.1016/0273-1177(93)90391-N. 27

Owens, M. J. (2006), Magnetic cloud distortion resulting from propagation through a structured solar wind: Models and observations, *J. Geophys. Res. (Space Phys.)*, *111*, A12,109, doi:10.1029/2006JA011903. 15, 16, 17, 18

Parker, E. N. (1958), Dynamics of the Interplanetary Gas and Magnetic Fields., *Astrophys. J.*, *128*, 664. 1, 2

Romashets, E. P., and M. Vandas (2003), Force-free field inside a toroidal magnetic cloud, *Geophys. Res. Lett.*, *30*(20), 200,000–1, doi:10.1029/2003GL017692. 13

Russell, C. T., and T. Mulligan (2002), On the magnetosheath thicknesses of interplanetary coronal mass ejections, *Planet. Space Sci.*, *50*, 527–534. 18, 19, 40, 43, 50

Shimazu, H., and M. Vandas (2002), A self-similar solution of expanding cylindrical flux ropes for any polytropic index value, *Earth, Planets, and Space*, *54*, 783–790. 13, 28

Siscoe, G., and D. Odstrcil (2008), Ways in which ICME sheaths differ from magnetosheaths, *J. Geophys. Res. (Space Phys.)*, *113*, 0–+, doi:10.1029/2008JA013142. 13, 40, 50, 57

Sonnerup, B. U. O., and L. J. Cahill, Jr. (1967), Magnetopause Structure and Attitude from Explorer 12 Observations, *J. Geophys. Res.*, *72*, 171–+, doi:10.1029/JZ072i001p00171. 12

Vandas, M., and E. P. Romashets (2003), A force-free field with constant alpha in an oblate cylinder: A generalization of the Lundquist solution, *Astronomy and Astrophysics*, *398*, 801–807, doi:10.1051/0004-6361:20021691. 33, 35, 36

Vandas, M., E. P. Romashets, S. Watari, A. Geranios, E. Antoniadou, and O. Zacharopoulou (2006), Comparison of force-free flux rope models with observations of magnetic clouds, *Advances in Space Research*, *38*, 441–446, doi:10.1016/j.asr.2004.11.026. 13, 27

Wang, C., and J. D. Richardson (2004), Interplanetary coronal mass ejections observed by Voyager 2 between 1 and 30 AU, *J. Geophys. Res. (Space Phys.)*, *109*, 6104–+, doi:10.1029/2004JA010379. 7, 25, 43

Wimmer-Schweingruber, R. F., et al. (2006), Understanding Interplanetary Coronal Mass Ejection Signatures. Report of Working Group B, *Space Sci. Rev.*, *123*, 177–216, doi:10.1007/s11214-006-9017-x. 7

Wood, B. E., and R. A. Howard (2009), An Empirical Reconstruction of the 2008 April 26 Coronal Mass Ejection, *Astrophys. J.*, *702*, 901–910, doi:10.1088/0004-637X/702/2/901. 5

REFERENCES

Xie, H., O. C. St. Cyr, N. Gopalswamy, S. Yashiro, J. Krall, M. Kramar, and J. Davila (2009), On the Origin, 3D Structure and Dynamic Evolution of CMEs Near Solar Minimum, *Sol. Phys.*, *259*, 143–161, doi:10.1007/s11207-009-9422-x. 5

Zurbuchen, T. H., and I. G. Richardson (2006), In-Situ Solar Wind and Magnetic Field Signatures of Interplanetary Coronal Mass Ejections, *Space Sci. Rev.*, *123*, 31–43, doi:10.1007/s11214-006-9010-4. 7

Appendix: List of publications

A1: Lynnyk, A., Vandas, M. (2009), Fitting of expanding magnetic clouds: A statistical study, *Planet Space Sci.*, 57 (12): 13751380. doi:10.1016/j.pss.2009.06.015

A2: Lynnyk, A., Vandas, M. (2010), Influence of Magnetic Cloud Expansion on Its Fits, *AIP Conf. Proc.*, 1216: 395398. doi:10.1063/1.3395885

A3: Lynnyk, A., Šafránková, J., Němeček, Z., Richardson, J. D., Deformation of ICMEs/MCs along their path, *Planet Space Sci.*, 59 (9): 840847. doi:10.1016/j.pss.2011.03.016

A1 - Lynnyk and Vandas (2009)

Lynnyk, A., Vandas, M. (2009), Fitting of expanding magnetic clouds: A statistical study, *Planet Space Sci.*, 57 (12): 13751380. doi:10.1016/j.pss.2009.06.015

A2 - Lynnyk and Vandas (2010)

Lynnyk, A., Vandas, M. (2010), Influence of Magnetic Cloud Expansion on Its Fits, *AIP Conf. Proc.*, 1216: 395398. doi:10.1063/1.3395885

A3 - Lynnyk et al. (2011)

Lynnyk, A., Šafránková, J., Němeček, Z., Richardson, J. D., Deformation of ICMEs/MCs along their path, *Planet Space Sci.*, 59 (9): 840847. doi:10.1016/j.pss.2011.03.016